



HAL
open science

**Observations of the south seasonal cap of Mars during
recession in 2004–2006 by the OMEGA
visible/near-infrared imaging spectrometer on board
Mars Express**

Yves Langevin, Jean-Pierre Bibring, Franck Montmessin, François Forget, M.
Vincendon, Sylvain Douté, F. Poulet, Brigitte Gondet

► **To cite this version:**

Yves Langevin, Jean-Pierre Bibring, Franck Montmessin, François Forget, M. Vincendon, et al.. Observations of the south seasonal cap of Mars during recession in 2004–2006 by the OMEGA visible/near-infrared imaging spectrometer on board Mars Express. *Journal of Geophysical Research. Planets*, 2007, 112 (E8), pp.E08S12. 10.1029/2006JE002841 . insu-00359439

HAL Id: insu-00359439

<https://insu.hal.science/insu-00359439>

Submitted on 16 Jun 2019

HAL is a multi-disciplinary open access archive for the deposit and dissemination of scientific research documents, whether they are published or not. The documents may come from teaching and research institutions in France or abroad, or from public or private research centers.

L'archive ouverte pluridisciplinaire **HAL**, est destinée au dépôt et à la diffusion de documents scientifiques de niveau recherche, publiés ou non, émanant des établissements d'enseignement et de recherche français ou étrangers, des laboratoires publics ou privés.

Observations of the south seasonal cap of Mars during recession in 2004–2006 by the OMEGA visible/near-infrared imaging spectrometer on board Mars Express

Y. Langevin,¹ J.-P. Bibring,¹ F. Montmessin,² F. Forget,³ M. Vincendon,¹ S. Douté,⁴ F. Poulet,¹ and B. Gondet¹

Received 7 October 2006; revised 8 December 2006; accepted 19 January 2007; published 21 July 2007.

[1] The OMEGA visible/near-infrared imaging spectrometer on board Mars Express has observed the southern seasonal cap in late 2004 and 2005 and then in the summer of 2006. These observations extended from the period of maximum extension, close to the southern winter solstice, to the end of the recession at L_s 325°. The spectral range and spectral resolution of OMEGA make it possible to monitor the extent and effective grain size of CO₂ ice and H₂O ice on the ground, the level of contamination of CO₂ ice and H₂O ice by dust, and the column density of μm -sized ice grains in the atmosphere. The CO₂ seasonal cap is very clean and clear in early southern winter. Contamination by H₂O ice spreads eastward from the Hellas basin until the southern spring equinox. During southern spring and summer, there is a very complex evolution in terms of effective grain size of CO₂ ice and contamination by dust or H₂O ice. H₂O ice does not play a significant role close to the southern summer solstice. Contamination of CO₂ ice by H₂O ice is only observed close to the end of the recession, as well as the few H₂O ice patches already reported by Bibring et al. (2004a). These observations have been compared to the results of a general circulation model, with good qualitative agreement on the distribution of H₂O ice on the surface and in the atmosphere. Resolving the remaining discrepancies will improve our understanding of the water cycle on Mars.

Citation: Langevin, Y., J.-P. Bibring, F. Montmessin, F. Forget, M. Vincendon, S. Douté, F. Poulet, and B. Gondet (2007), Observations of the south seasonal cap of Mars during recession in 2004–2006 by the OMEGA visible/near-infrared imaging spectrometer on board Mars Express, *J. Geophys. Res.*, 112, E08S12, doi:10.1029/2006JE002841.

1. Introduction

[2] The seasonal caps of Mars play an important role in the seasonal cycle as a trap for a major fraction of atmospheric gases, in particular CO₂ and H₂O [Jakosky, 1985; James et al., 1992]. The relationship between seasonal cap characteristics and atmospheric circulation models has been investigated by several authors [Forget et al., 1999; Colaprete et al., 2005]. Near IR spectrometry [Herr and Pimentel, 1969; Larson and Fink, 1972; Calvin and Martin, 1994] and observations in the thermal IR [Neugebauer et al., 1971; Kieffer, 1979; Kieffer et al., 2000] have demonstrated that CO₂ ice is the major component of the seasonal caps. Observations in the visible [James et al., 1987; Benson and James, 2005] associated with observations by the

thermal emission spectrometer (TES) on board MGS [Kieffer et al., 2000] have provided information on the recession of the south seasonal cap over a wide range of Martian years. A temperature <145 K is a reliable diagnostic of the presence of CO₂ ice, as it corresponds to the sublimation temperature in Martian conditions. However, contamination of CO₂ ice by dust or H₂O ice cannot be detected in the thermal IR. Bright areas with higher temperatures (160–170 K) have been considered to be covered by H₂O ice. This is in particular the case for the perennial northern polar cap [Kieffer et al., 1976; Kieffer and Titus, 2001]. During northern spring, a moderately cold and bright ring lagging a few degrees of latitude behind the receding boundary of regions at CO₂ sublimation temperatures has been observed by TES and interpreted as H₂O frost [Kieffer and Titus, 2001]. This has been recently confirmed by a direct spectral identification from near-IR observations by the OMEGA near-IR infrared spectrometer on board Mars Express [Bibring et al., 2005].

[3] The advance and recession of the south seasonal cap has been monitored by TES over two Martian years [Kieffer et al., 2000; Titus and Kieffer, 2002]. The thermal boundary reaches its maximum extent from a heliocentric longitude (or L_s) of 90° (southern winter solstice) to L_s 120°. A H₂O frost recondensation process similar to what is observed in

¹Institut d'Astrophysique Spatiale, CNRS/Université Paris Sud, Orsay, France.

²Service d'Aéronomie, CNRS/Université Pierre et Marie Curie, Verrières-le-Buisson, France.

³Laboratoire de Météorologie Dynamique, CNRS/Université Pierre et Marie Curie, Paris, France.

⁴Laboratoire de Planétologie de Grenoble, CNRS/Université Joseph Fourier, Grenoble, France.

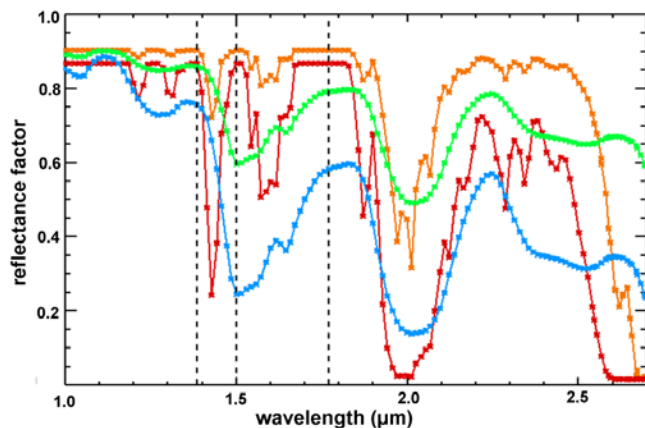


Figure 1. Model spectra of CO₂ ice with grain sizes of 1 mm (orange) and 5 cm (red) and H₂O ice with grain sizes of 10 μm (green) and 100 μm (blue). The three dashed lines correspond to the OMEGA spectels at 1.385 μm, 1.5 μm, and 1.77 μm which are used for the determination of the strength of the H₂O ice absorption band at 1.5 μm, as there are only weak CO₂ absorption features at these wavelengths.

the north is predicted by global circulation models for the recession of the southern seasonal cap [Houben et al., 1997; Montmessin et al., 2004]. A few spectra of the south circumpolar regions at wavelengths longer than 1.8 μm had been obtained by the Mariner 7 infrared spectrometer during its Mars flyby on 4 August 1969 ($L_s \sim 202^\circ$). These observations provided evidence for a minor contamination of the south seasonal cap by H₂O ice from an increase in the 3 μm absorption [Herr and Pimentel, 1969]. However, no clear evidence for a H₂O frost ring has yet been obtained around the retreating southern seasonal cap. A single occurrence of a 15 km × 70 km region with similar temperature/albedo characteristics as the northern H₂O frost ring has recently been reported close to the south pole at $L_s 260^\circ$ – 270° (close to the southern summer solstice) from combined observations of TES and the THEMIS thermal IR imaging spectrometer on board Mars Odyssey [Titus, 2005a]. Therefore few observational constraints were available on the role of the southern seasonal cap in the water seasonal cycle of Mars.

[4] The OMEGA Vis/NIR imaging spectrometer aboard Mars Express [Bibring et al., 2004b] has provided the first comprehensive coverage of the Martian surface from 0.35 μm to 5.1 μm [Bibring et al., 2005]. Unambiguous signatures of H₂O ice and CO₂ ice are observed in this wavelength range (Figure 1), with diagnostic absorption bands at 1.25 μm, 1.5 μm, 2 μm and 3 μm (H₂O ice), 1.435 μm, 2.281 μm, 2.7 μm and 3.3 μm (CO₂ ice) [Grundy and Schmitt, 1998; Quirico and Schmitt, 1997; Hansen, 2005]. A correction method for major and minor atmospheric CO₂ bands has been presented as supplementary material by Langevin et al. [2006].

[5] The strength of the bands associated to solid CO₂ and H₂O increases with the mean path length of photons within the upper surface layers. The mean path length is itself inversely related to the volume density of the scattering interfaces: grain boundaries/fractures, inclusions of dust or

H₂O ice (within CO₂ ice). Even low levels of dust contamination have a drastic impact on albedo and band strength for ice layers dominated either by H₂O or CO₂ ice. Radiative transfer models with single or multiple layers [Douté and Schmitt, 1998; Poulet et al., 2002] can therefore be used to constrain the characteristics of the icy surface. Such analyses have already been performed on OMEGA data for the south perennial cap [Bibring et al., 2004a; Douté et al., 2007], the north perennial cap [Langevin et al., 2005], the north seasonal cap [Schmitt et al., 2005] and the “cryptic region” of the south seasonal cap [Langevin et al., 2006].

[6] In this contribution, we report on observations of the south seasonal cap by OMEGA from mid 2004 to mid 2006. These observations provide a comprehensive coverage of the evolution of the south seasonal cap from its maximum extension close to the south winter solstice ($L_s 90^\circ$) to the end of the recession at $L_s \sim 325^\circ$. A series of 30 maps have been obtained for three important parameters: the albedo in the continuum, which is controlled by dust contamination, the spectral signature of CO₂ ice and the spectral signature of H₂O ice which are most diagnostic of seasonal ice characteristics.

[7] The spatial distribution of H₂O ice as a function of L_s is a signature indicator of weather patterns on Mars. The observed maps have been compared with the predictions of a Global Circulation Model [Forget et al., 1999; Montmessin et al., 2004]. This comparison demonstrates that these models are able to account for many key characteristics of the evolution of southern high latitudes. However, there are significant discrepancies. The resolution of these remaining issues will help in further improving and constraining climate models of Mars.

2. Observation Conditions

[8] The evolution of the elliptical orbit of Mars Express, which is nearly polar (inclination $\sim 86.6^\circ$) is a major constraint for OMEGA observations, as they can only be performed over sunlit areas (contrary to observations in the thermal IR). The S/N ratio improves and the impact of aerosols decreases when the Sun is high above the horizon: no meaningful observations of the surface can be obtained for incidence angles higher than 86° , and optimal conditions require incidence angles lower than 60° . Furthermore, the pixel size is proportional to the altitude of the spacecraft. The pericenter of the orbit precesses backward relative to the motion of the spacecraft due to the significant quadrupole term (J_2) of the gravity field of Mars. After a full Martian year, it has moved by 435° ; hence the pericenter has shifted by $\sim 75^\circ$ in latitude at the same heliocentric longitude L_s . The local time at pericenter changes continuously due to the angular orbital motion of the planet combined with a slow precession of the orbit plane. Figure 2 shows the position of the orbit of Mars Express and the relationship with the position of the Sun at different dates during the observations of the south seasonal cap. This figure demonstrates the wide range of local times and altitudes of OMEGA observations of the southern high latitudes. The local time is particularly critical for mid southern latitudes, as regions close to the terminator can only be observed at high solar incidence angles. It is a less critical parameter for

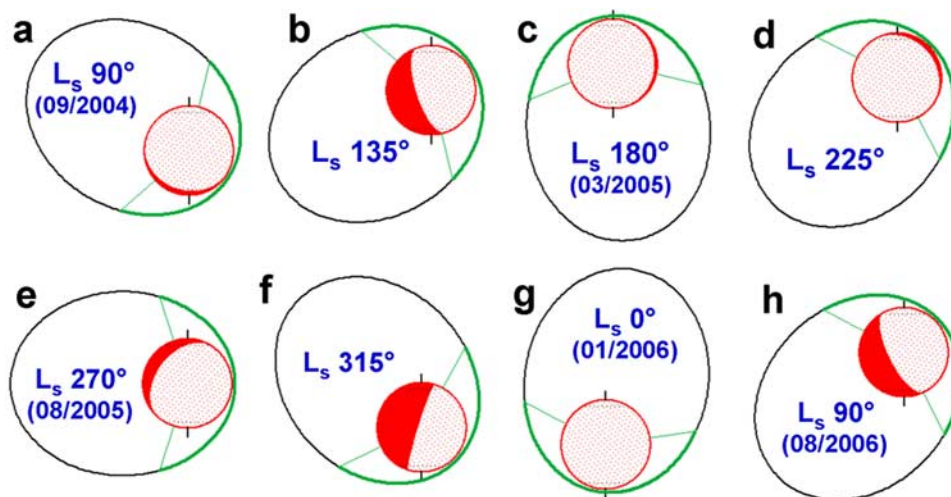


Figure 2. Orbit of Mars Express during OMEGA observations of the southern seasonal cap for eight values of the heliocentric longitude L_s from the southern winter solstice of Martian year 27 (Figure 2a) to the end of the recession (shortly after $L_s 315^\circ$, Figure 2f) the southern fall equinox (Figure 2g) and the southern winter solstice of Martian year 28 (Figure 2h). The arc between the two thin lines connecting the orbit to the planet indicate altitudes below 4500 km, which corresponds to the range of true anomalies over which observations with nadir pointing are possible. Beyond this altitude range, observations are performed in a 3-axis drift mode. The sunlit part of the planet is shown as seen from a direction perpendicular to the orbit plane.

very high latitudes, for which sun elevation is mostly controlled by the seasonal cycle. Nadir pointing is the nominal mode for altitudes <4500 km. Observations are performed in a 3-axis “drift” mode for altitudes ranging from 4500 km to 10,000 km (apocenter). OMEGA observations at altitudes >1400 km are swaths 128 pixels wide with an IFOV of 1.2 mrad, extending over 215 km to 1500 km with an IFOV of 1.7 km to 12 km depending on altitude. Consecutive swaths can be summed on board at high altitudes so as to minimize oversampling. At altitudes <1400 km, the 128 pixels observation mode would result in increasingly severe undersampling as the drift time across a pixel decreases. The swath width is therefore adjusted to 64 pixels, then 32 pixels and finally 16 pixels as the altitude decreases. The orbital period of Mars Express is close to the 11:3 resonance. This means that after 11 orbits and 3 sols, the subspacescraft track returns to the same region with a small longitudinal shift. Eleven different longitude zones can be observed during a cycle. The 3 sols cycle represents the maximum temporal resolution of sequences of OMEGA observations except at very high latitudes (where all 11 swaths can overlap). A series of 11 observations (which can be selected from several consecutive cycles) provides the most comprehensive coverage available for a given period in nadir pointing mode. The latitudes over which swaths overlap depend on the orbital configuration (which controls the altitude). If the altitude over the south pole is lower than 2600 km, the highest latitudes can no longer be observed with nadir pointing, as the subspacescraft track lies 200 km away from the pole.

[9] The configuration near the maximum extent of the seasonal cap in the early fall of 2004 was extremely unfavorable, as the orbit was close to the terminator (Figure 2a). No observations were possible during the solar conjunction

period ($L_s 80^\circ$ to $L_s 95^\circ$). Furthermore, the spacecraft altitude over the mid southern latitudes corresponding to the boundary of the seasonal cap in this period was lower than 500 km, which reduced coverage to a track less than 8 km wide. The first extensive observations of the south seasonal cap by OMEGA were therefore performed using the nominal nadir pointing mode in late 2004 and early 2005 ($L_s 130^\circ$ – $L_s 154^\circ$) when the pericenter had moved north and the local time was more favorable (Figure 2b).

[10] From $L_s 155^\circ$ to $L_s 235^\circ$, the pericenter was at high northern latitudes; hence south polar regions could only be observed in 3-axis pointing mode. Two sets of observations were performed in this period:

[11] 1. A comprehensive set of 11 orbits was obtained so as to cover the whole southern seasonal cap as soon as the Sun rose over the south pole, shortly after the southern spring equinox ($L_s 184^\circ$ – 193° , close to the situation of Figure 2c). This is the only set observations for which regions of the seasonal cap are observed with an emergence angle larger than 25° (up to 60° at the south pole).

[12] 2. A second set of observations was performed in midspring ($L_s 221.4^\circ$ to $L_s 224.3^\circ$, Figure 2d) as this period corresponds to the maximum contrast of the inner dark zone known as the “cryptic region” [Kieffer *et al.*, 2000]. These observations have already been discussed by Langevin *et al.* [2006]. The selected 3-axis pointing mode resulted in emergence angles ranging from 0° to 25° over most of the seasonal cap.

[13] After $L_s 237^\circ$, the observation conditions became very favorable, as nadir observation could be resumed and high southern latitudes became permanently illuminated. 18 sets of observations could be obtained until $L_s \sim 285^\circ$, providing extensive coverage at intervals of ~ 6 days. During this period, the pericenter was moving south

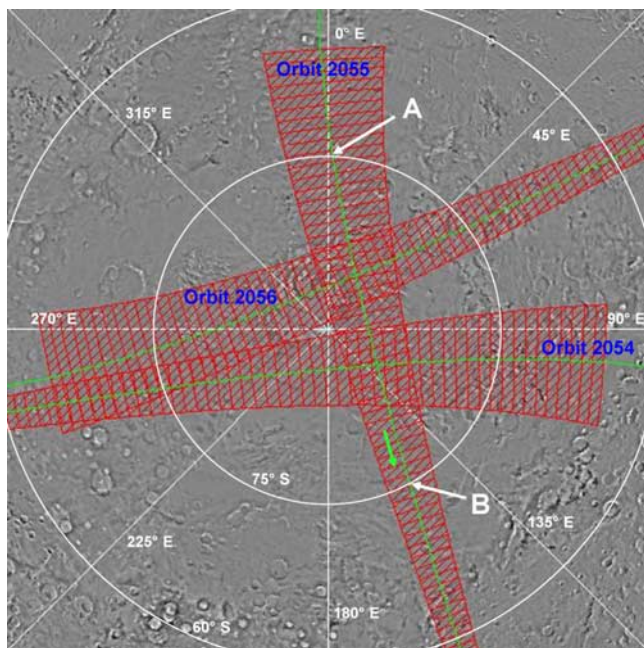


Figure 3. Observation strategy with nadir pointing close to L_s 273° (Mars Express orbits 2054 to 2064; see Table 1) which corresponds to a very favorable period in terms of downlink capability. The extent of the 128 pixel swath of OMEGA is displayed as red outlines for the first three orbits of this set of 11 orbits corresponding to almost exactly 3 sols, starting when the Sun is 10° above the horizon. Each latitude from 65°S to the pole can be observed twice: first at high incidence and high altitude, hence a large pixel size, when the Mars Express spacecraft comes in from the nightside, and then at a lower incidence and altitude, hence a smaller pixel size, when it moves on toward the pericenter on the dayside. For regions at a latitude of 75°S, the pixel size is first ~ 4 km with an incidence of 73° (A), and then ~ 1.9 km with an incidence of 53° (B). At closest approach to the pole, the pixel size is 3 km, so that 64 pixels cover 192 km, and the swath almost (but not quite) reaches the south pole, which is 200 km away from the sub-spacecraft track (green line). The three consecutive orbits 2054, 2055, and 2056 adequately covered latitudes from 85°S to the pole. The 9 observations obtained by OMEGA over the 11 orbit cycle (only 2058 and 2062 were missed due to downlink constraints) provided a comprehensive coverage down to 75°S. Orbit 2065 covered nearly the same regions as orbit 2054, starting a new cycle. This figure has been produced using the “MAPPS” tool (P. Van der Plas, © ESA/ESTEC), which is provided to Mars Express PI teams for science planning.

(Figure 2e); hence the IFOV improved (3 km at the pole at $L_s \sim 270^\circ$), but the swaths were getting narrower. A nearly comprehensive coverage could however be maintained, as this evolution was nearly in phase with the recession of the south seasonal cap. In the latter part of the period, the half-width of the swath at the pole was lower than 200 km, resulting in a small gap in coverage for the highest latitudes. The observation strategy at $L_s \sim 273^\circ$, the last set of OMEGA observations which reaches the highest latitudes with nadir pointing, is presented in Figure 3. After L_s 285°,

the width of the swath reduced even further due to the low altitude of the pericenter (< 800 km at the south pole, Figures 2f and 2g). The coverage could be increased by implementing off-nadir pointing, but there were still gaps between successive orbits, in particular at very high latitudes. A series of seven partial maps were obtained until L_s 325° with an IFOV of 2 km down to 700 m so as to monitor the last stages of the recession of the south cap until it reached the boundaries of the perennial CO_2 cap. For such very small IFOVs, the observations were repositioned with respect to Viking HR mosaics compiled by USGS, so as to compensate for small time shifts and pointing offsets between reconstructed and actual positions and orientations of the Mars Express spacecraft. Viking mosaics have also been used as background for maps of band depths so as to provide the context of OMEGA observations.

[14] A final set of nadir pointing observations was obtained in late July/early August 2006 (L_s 86°–94°) with good observation conditions (Figure 2h) so as to obtain information on the period close to the southern winter solstice, which could not be observed in 2004. The season of long eclipses starting in late August 2006 prevented observations to be performed at the period of maximum extension of the cap ($L_s \sim 105^\circ$). It should however be noted that at L_s 90°, the southern seasonal cap is already within 1° of latitude of its maximum extension as observed by TES [Titus and Kieffer, 2002]. This set of observations can therefore be considered as representative of the maximum extension of the seasonal cap.

3. Selection of the Most Relevant Parameters for Monitoring the Evolution of the Southern Seasonal Cap

3.1. Albedo in the Continuum

[15] The first relevant parameter to be monitored is the reflectance factor (Lambert albedo) in the continuum. The reflectance factor corresponds to the ratio of the observed radiance to the incoming solar flux per unit of surface, which is proportional to the cosine of the incidence angle. It

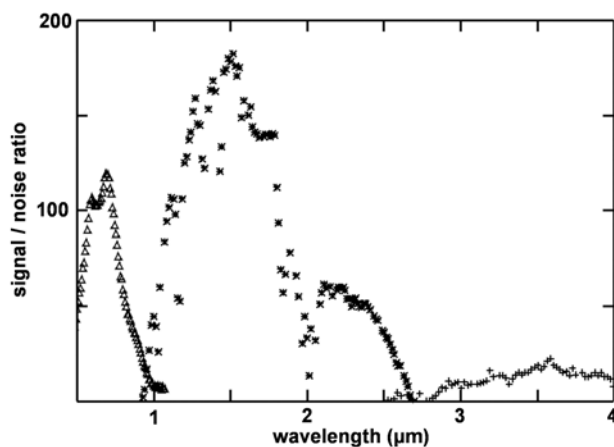


Figure 4. Signal-to-noise ratio of OMEGA as a function of wavelength for a relatively dark region (albedo $\sim 18\%$ at $1.08 \mu\text{m}$) observed at high incidence angles (80°), close to aphelion (1.66 AU).

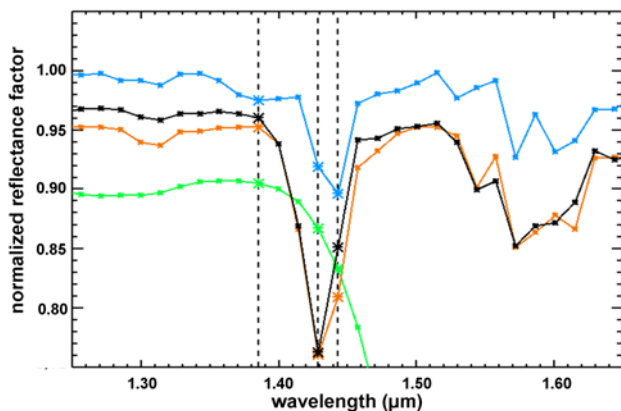


Figure 5. Atmospheric absorption (blue), model H₂O ice spectrum (green), model spectrum of CO₂ ice with a grain size of 1 mm (orange), and observed CO₂ ice spectrum (black) from 1.25 μm to 1.65 μm . Each symbol corresponds to a single OMEGA spectral element. The three dashed lines correspond to wavelengths of 1.385 μm , 1.429 μm , and 1.443 μm , which are used for the determination of the strength of the CO₂ ice absorption at 1.435 μm . The spectral elements at 1.46 μm and higher would be out of the 1.435 μm CO₂ ice feature (orange spectrum), but they lie too deep in the H₂O ice absorption feature (green spectrum) to be used for a reliable determination of the CO₂ ice band strength in seasonal frosts associating the two types of ices.

does not depend on the incidence and emergence angles for strongly scattering surfaces with a distribution of outgoing photons similar to that of blackbody radiation (proportional to the cosine of the emergence angle). The bright albedo of high-latitude regions in winter provided the first evidence for seasonal caps. Comprehensive observations of the advance and the recession of the south seasonal cap from Mars orbit were first performed on the basis of the albedo in the visible during the Viking mission [James *et al.*, 1979]. The visible albedo was also monitored by the cameras on board MGS [Benson and James, 2005] and the broadband channel of TES [Kieffer *et al.*, 2000]. It is therefore important to monitor the Lambert albedo in the continuum so as to compare OMEGA observations in 2004–2006 to previous observations of the south seasonal cap. Furthermore, the albedo in the continuum is the most critical parameter for monitoring the contribution of dust to spectral characteristics of icy surfaces. This contribution results from a complex combination of absorption and scattering by aerosols, dust on the surface at subpixel scales (from individual grains to patches a few hundreds of meters in size for OMEGA), and dust contamination of the ice itself (either at grain boundaries or embedded within ice grains).

[16] The OMEGA spectral range extends from 0.36 μm to 5.09 μm [Bibring *et al.*, 2004b]. It is covered by a visible channel (96 wavelengths from 0.36 μm to 1.07 μm) and two IR channels (C: 128 wavelengths from 0.92 μm to 2.7 μm ; L: 128 wavelengths from 2.53 μm to 5.09 μm). The signal-to-noise available for an observation of a region at a latitude of 50°S in worst case conditions (Lambert albedo of 18%, 80° incidence angle, Mars at 1.66 AU, close to aphelion, no swath summation) is shown in Figure 4 for all three channels. Even then, the S/N exceeds 50 for most of the

C channel and part of the visible channel. The S/N of OMEGA is read noise limited, which means that it increases linearly with the solar flux (controlled by the incidence angle and heliocentric distance) and the albedo (up to 80% for ice covered regions). Swath summation (2 or 4) further increases the S/N (by 1.4 or 2) at altitudes >2400 km. Therefore the stochastic S/N exceeds 1000 at 1.5 μm for a major fraction of OMEGA observations of the seasonal cap. This very high S/N is relevant for comparing spectra within a given swath. Small time-dependent deviations from linearity can result in instrumental errors on the order of 1% when comparing spectra from different swaths.

[17] After 5 months in orbit (June 2004), data became corrupted every 32 spectral elements (or “spectels”) for pixels 80 to 95 of swaths 128 pixels wide. Avoiding these spectral regions is therefore required so as to benefit from the full extent of these swaths until early September 2005, when the whole second half of these swaths (pixels 64 to 127) became corrupted in a similar way. Two regions can be considered for evaluating the reflectance factor in the continuum when considering these instrumental problems, the S/N dependence on wavelength (Figure 4) and the spectral absorption features of ices (Figure 1): close to 0.7 μm in the visible channel and close to 1.1 μm in the C channel. The visible channel presents an elongated IFOV, extending ~ 4 mrad in the cross-slit direction (compared to 1.2 mrad along the slit) and aerosol effects become less severe as the wavelength increases. Therefore we selected a spectel at 1.08 μm in the C channel for mapping the Lambert albedo in the continuum.

[18] As demonstrated by the albedo maps in section 4, the Lambert scattering assumption provides acceptable mosaics of the high-latitude regions in most cases. This is surprising as icy surfaces can depart significantly from a Lambert emission law if specular reflection becomes significant. Furthermore, aerosol extinction can be a major factor as incidence angles are high for southern polar regions (at best 65.1° at the south pole itself). Thick slabs of CO₂ ice overlying the surface such as that observed at 60°S in winter [Langevin *et al.*, 2006] are expected to introduce a dependence of the reflectance factor on the incidence angle, as photons undergoing specular reflection at the interface are lost for Nadir pointing observations. The refractive index of CO₂ ice is ~ 1.4 in the near-IR [Warren, 1986]. From Fresnel’s law, the effective solar flux is reduced by up to 15% at an incidence angle of 70° and by up to 36.7% at an incidence angle of 80° if the CO₂ ice slab is perfectly clean and flat. Once photons enter the CO₂ layer, if the underlying surface is Lambertian, the outgoing flux will also be Lambertian after refraction at the interface. The impact of aerosol extinction and scattering on observed spectra is discussed by Vincendon *et al.* [2006] and in section 3.4.

3.2. CO₂ Ice

[19] CO₂ ice dominates the composition of the southern seasonal cap, as demonstrated by measurements in the thermal IR [Kieffer, 1979; Kieffer *et al.*, 2000]. It is important to monitor the extent of areas presenting CO₂ ice signatures so as to compare them with albedo and temperature contrasts. As demonstrated by Figure 1, several minor and major CO₂ ice absorption bands can be observed

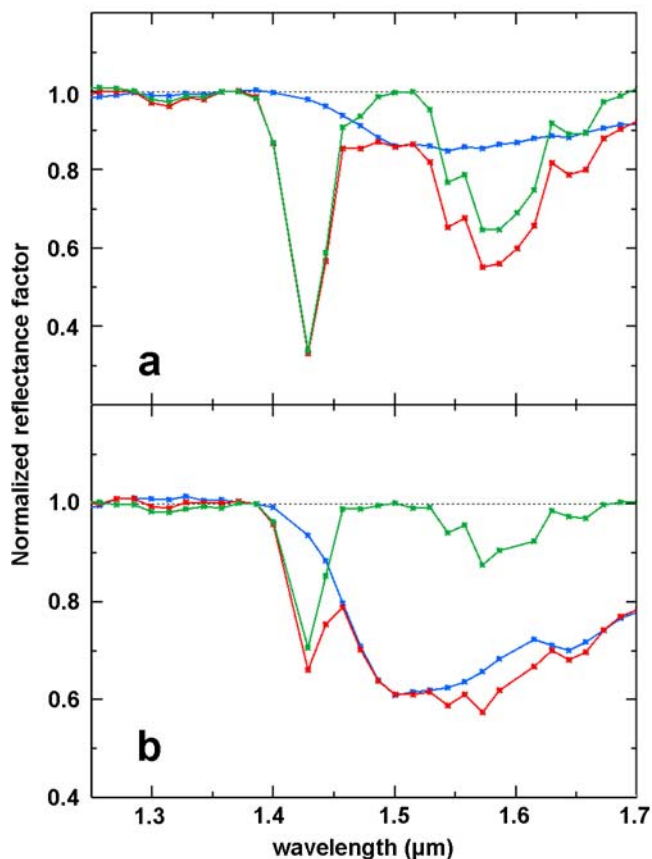


Figure 6. Evaluation of the CO₂ ice band strength at 1.435 μm when H₂O frost is present. Normalized reflectance spectra (1.25 to 1.7 μm) obtained by OMEGA are presented for high-latitude regions of Mars exhibiting signatures of seasonal frost. The red spectra exhibit both the CO₂ ice and H₂O ice spectral signatures. Blue spectra correspond to areas which exhibit no CO₂ ice signature and the same H₂O ice band strength at 1.5 μm as the red spectrum. The green spectra are obtained by dividing the red spectrum by the corresponding blue spectrum. They provide an estimate of the actual band strength of the CO₂ ice absorption feature at 1.425 μm: 0.67 for the region of Figure 6a (spectrally dominated by CO₂ ice) and 0.29 for the region of Figure 6b (spectrally dominated by H₂O ice). These estimates are very consistent with the values provided by the CO₂(1.435 μm) evaluator when applied on the red spectra (0.665 for Figure 6a and 0.297 for Figure 6b).

by OMEGA. The strength of the bands depend on the path length of photons within CO₂ ice, which is related to the mean distance between interfaces (grain boundaries, fractures) and the density of scattering particles (e.g., dust inclusions) within CO₂ ice. The band strengths can therefore provide information on texture and contamination by dust grains or H₂O ice crystals. Path lengths of photons in CO₂ ice as observed by OMEGA on Mars can reach values of several tens of centimeters. Minor bands which are not saturated are therefore best suited for obtaining this information. The 2 μm band overlaps with absorptions due to atmospheric CO₂. This is also in part the case for the 2.7 μm

band. Furthermore, this very strong absorption band saturates for most OMEGA observations; hence its depth cannot be used to constrain the photon path length. The depth and shape of the 3.3 μm band is a very good diagnostic of path length, but it is overlapped toward short wavelengths by the very strong 3 μm absorption band of H₂O ice, so that even a minor contamination by H₂O ice has a major impact on band shapes in this spectral region. Furthermore, spectral identifications are made more complex by the low S/N (Figure 4) and the deep hydration band at 3 μm which is observed for all surface materials as well as in aerosols [Jouglet *et al.*, 2007; Milliken *et al.*, 2007]. The C channel (0.92 μm to 2.7 μm) has been very stable since launch in terms of wavelengths and photometric response. The narrow absorption at 1.435 μm (Figure 1) provides the best S/N ratio among minor CO₂ ice bands which do not saturate except for the largest observed path lengths (>20 cm). It lies close to the optimum of the photometric function of OMEGA (Figure 4). The next strongest minor CO₂ ice feature lies at 2.281 μm. It is a factor of 2.3 weaker than the 1.435 μm feature, and the signal is typically 3 times lower in this spectral range than at 1.435 μm; hence the S/N on band strength is a factor of 7 lower at 2.281 μm than at 1.435 μm. Therefore we selected the 1.435 μm absorption for evaluating the strength of CO₂ ice absorption features.

[20] The 1.435 μm absorption of CO₂ ice lies very close to a minor absorption feature of atmospheric CO₂ (~1.44 μm). It is also overlapped by the short wavelength edge of the broad absorption feature of H₂O ice which extends from 1.38 μm to 1.8 μm (Figure 1). A specific evaluator has been selected so as to minimize the impact of these absorption features. It is derived from the ratio *R* of the reflectance factor at 1.429 μm relative to that at 1.385 μm and 1.443 μm:

$$R = \text{RF}(1.429 \mu\text{m}) / \left(\text{RF}(1.385 \mu\text{m})^{0.5} \times \text{RF}(1.443 \mu\text{m})^{0.5} \right)$$

[21] *R* is a reflectance ratio; hence (1 - *R*) is dimensionally equivalent to a band strength. (1 - *R*) is very close to 0 for modeled and observed spectra of pure H₂O ice frost (Figure 5), so that large admixtures of H₂O frost have a only a small impact on this parameter. Thanks to the small wavelength shift between CO₂ ice and atmospheric CO₂ absorption features, the impact of absorption by atmospheric CO₂ on (1 - *R*) is less than 2%, so that the variations in atmospheric band strengths resulting from altitude differences (typically 2 km in the southern high-latitude regions) can be neglected as the observed CO₂ ice band strengths can reach 80%. The spectral at 1.443 μm lies within the absorption feature, not in the continuum. Therefore (1 - *R*) underestimates the strength of the band. For regions free of H₂O ice, the full CO₂ ice band strength can be evaluated from a continuum at 1.385 μm and 1.486 μm on a ratio between the spectrum of a CO₂ ice covered region and that of a nearby ice free region at a similar altitude. The comparison between these observed band strengths and the corresponding values of (1 - *R*) led to the following evaluator for the strength of the CO₂ ice band at 1.435 μm:

$$\text{CO}_2(1.435 \mu\text{m}) = 1.16(1 - R)^{0.92}$$

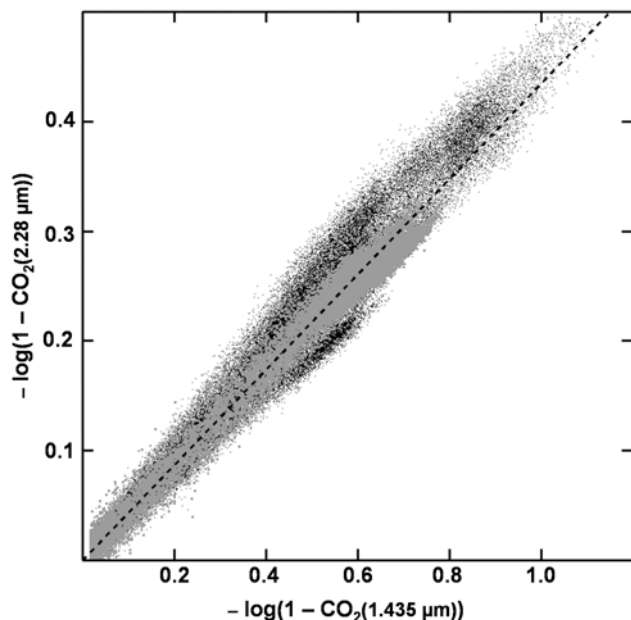


Figure 7. Extinction coefficient of the CO₂ ice bands at 1.435 μm and 2.281 μm for two observations at L_s 224° (black dots) and L_s 262° (grey stars). The dashed line corresponds to a ratio of 2.3 between the strength of the two absorptions. This parameter is expected to scale with the path length within CO₂ ice. The correlation is excellent (0.997) close to the southern summer solstice, when incidence angles are relatively low, which reduces the impact of aerosol scattering. The few observations which saturate at 1.4 μm are all close to summer solstice due to the high signal levels in this period.

If $(1 - R)$ is smaller than 0.01, CO₂(1.435 μm) is set to 0 as this value corresponds to the upper limit for ice free soils. This evaluator has been validated on regions presenting signatures of both CO₂ and H₂O ices (Figure 6). It provides an adequate estimate of the band strength specific to CO₂ ice even when medium to strong H₂O ice absorption features are observed.

[22] A small fraction of OMEGA observations of the south seasonal cap reach detector saturation between 1.2 μm and 1.6 μm, where the raw signal is largest (Figure 4). In such cases, the CO₂ ice band strength at 1.435 μm cannot be estimated. It is then evaluated from the band strength CO₂(2.281 μm) of a minor feature at 2.281 μm (a wavelength range where the raw signal is 3 times lower). The band strength is estimated by comparing the reflectance factor at the OMEGA wavelength closest to the band center (2.287 μm) to that of a continuum evaluated at 2.287 μm from the reflectance factor at 2.219 μm and 2.314 μm:

$$\text{CO}_2(2.281 \mu\text{m}) = 1 - \text{RF}(2.287 \mu\text{m}) / \left(\text{RF}(2.219 \mu\text{m})^{0.3} \times \text{RF}(2.314 \mu\text{m})^{0.7} \right)$$

[23] For such non-saturated bands, the reflectance is expected to decrease exponentially with path length. There is indeed a fair to excellent correlation between the extinc-

tion coefficients for the 1.435 μm and the 2.281 μm bands, even with relatively poor observation conditions (Figure 7). The observed correlation corresponds to a ratio of 2.3 in band strength. One can then reliably derive the band strength at 1.435 μm, CO₂(1.435 μm), from the band strength at 2.281 μm, CO₂(2.281 μm) when the spectral region close to 1.4 μm is saturated:

$$\text{CO}_2(1.435 \mu\text{m}) = 1 - (1 - \text{CO}_2(2.281 \mu\text{m}))^{2.3}$$

[24] The CO₂(1.435 μm) parameter constrains the average path length within an IFOV. The relationship between non-saturated bands remains approximately valid even if there is substantial subpixel mixing of areas with very different path lengths. As an example, a 50% coverage by CO₂ ice within an OMEGA pixel with a strong extinction of 0.4 at 2.281 μm corresponds to an observed band strength of 0.165 at 2.281 μm and an observed band strength of 0.30 at 1.435 μm. A homogeneous zone with the same band strength at 2.281 μm (extinction of 0.165 over the whole pixel) would present only a small difference in band strength at 1.435 μm (0.34 instead of 0.3). Therefore the relative strength of non-saturated bands cannot easily be used to discriminate between large path lengths over a fraction of the pixel and smaller path lengths over the whole pixel. The presence of subpixel areas free of CO₂ ice is mainly constrained by the reflectance factor within saturated bands, in particular at wavelengths from 2.6 μm to 2.64 μm, out of major absorption bands of atmospheric CO₂. At near-IR wavelengths, this includes a significant contribution from the scattering of sunlight by ice-free aerosols. The issue of subpixel ice-free areas on the surface itself was already addressed by TES [Kieffer *et al.*, 2000]. These authors concluded that they do not play a major role for most of the evolution of the south seasonal cap, as its average temperature over scales of several km is close to the sublimation temperature of CO₂.

3.3. H₂O Ice

[25] H₂O ice has been observed at the boundary of the receding north seasonal cap first as a bright and moderately cold ring [Kieffer and Titus, 2001], then with a direct spectral identification by OMEGA [Bibring *et al.*, 2005]. As indicated in the introduction, there are as yet few identifications of H₂O ice in the southern seasonal cap. The inventory of regions of the south seasonal cap presenting H₂O ice signatures is therefore of interest for the water cycle on Mars. Many minor and major H₂O ice absorption bands can be monitored within the OMEGA wavelength range (0.35 to 5.1 μm). The strongest broad bands are located at wavelengths of 1.5 μm, 2 μm and 3 μm. The absorption band at 3 μm saturates when the path length of photons within H₂O ice exceeds a few μm, while longer paths are required for the 2 μm band (a few hundred μm) and the 1.5 μm band (~1 mm) [Grundy and Schmitt, 1998]. The range of grain sizes for H₂O ice on the surface lies between a few tens of μm (frost) and 1 mm (perennial northern ice cap) [Langevin *et al.*, 2005]. The 3 μm band is therefore not best suited to monitor the texture of surface ice, while it is a very sensitive indicator for even small

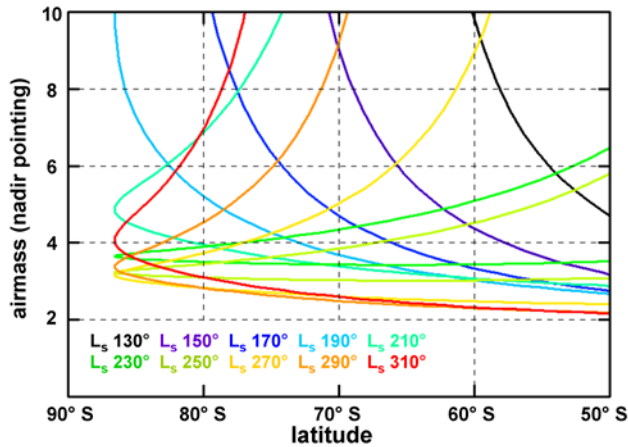


Figure 8. Total air mass evaluated with nadir pointing ($1 + 1/\cos(i)$) as a function of latitude for OMEGA observations at ten values of L_s at 20° intervals from 130° to 310° in late 2004 and 2005. No reliable observations can be made above an air mass of 10, as aerosol extinction and diffusion become a major factor even for low optical thickness conditions. Incidence angles higher than 85° have only been included for mapping the cap all the way to the south pole at $L_s 190^\circ$. The large air mass is then mitigated by the high altitude of these regions (up to 4 km above datum).

column densities of μm -sized H_2O ice grains in the atmosphere. Furthermore, similarly to the $3.3 \mu\text{m}$ CO_2 ice band, its analysis is complicated by the lower S/N (Figure 4) and the deep hydration band at $3 \mu\text{m}$ which is observed for all surface materials as well as in aerosols [Joulet *et al.*, 2007; Milliken *et al.*, 2007]. At wavelengths $\sim 2 \mu\text{m}$, there are strong CO_2 absorption features both in the solid state (Figure 1) and in the atmosphere. Therefore the $1.5 \mu\text{m}$ band is clearly best suited to monitor H_2O ice on the surface with OMEGA. This spectral range provides optimum S/N (Figure 4). It saturates only for very large grain sizes which are not expected for surface frost, and there are only very weak CO_2 absorptions (from either ice or gas) at the centre of the band (Figure 1). The evaluation of the band strength $\text{H}_2\text{O}(1.5 \mu\text{m})$ was made by comparing the reflectance factor at $1.5 \mu\text{m}$ to a continuum evaluated from the reflectance factor at two OMEGA wavelengths out of major CO_2 and H_2O absorption bands ($1.385 \mu\text{m}$ and $1.77 \mu\text{m}$), taking into account the different intervals between the center of the band and the selected continuum regions:

$$\text{H}_2\text{O}(1.5 \mu\text{m}) = 1 - \text{RF}(1.500 \mu\text{m}) / \left(\text{RF}(1.385 \mu\text{m})^{0.7} \times \text{RF}(1.772 \mu\text{m})^{0.3} \right)$$

[26] The $\text{H}_2\text{O}(1.5 \mu\text{m})$ evaluator significantly underestimates the band strength for large grain sizes, as there is already a significant absorption at $1.77 \mu\text{m}$ (Figure 1). However, this is not a critical issue for the relatively small grained surface H_2O frost ($<100 \mu\text{m}$) which is typical of

seasonal caps, and this approach minimizes the impact of aerosol diffusion, which is characterized by a blue slope in this wavelength range [Clancy *et al.*, 2003].

3.4. Impact of Aerosol Scattering and Extinction on Albedo Band Strengths

[27] Depending on their optical depth, aerosols can have a major impact on observed spectra [Erard *et al.*, 1994]. A fraction of photons are scattered by dust, multiple scattering playing a major role if the optical thickness is high [see, e.g., Ockert-Bell *et al.*, 1997]. Observations by the Mars Orbiter Camera [Wang and Ingersoll, 2002], MOLA [Neumann *et al.*, 2003] and TES [Smith *et al.*, 2001] have provided a consistent view of aerosol activity at southern latitudes. Widespread streak clouds are expected to cover a large fraction of midlatitude southern regions during mid southern winter [Wang and Ingersoll, 2002]. From the southern spring equinox to the southern solstice ($L_s 270^\circ$), haze is observed in the visible, as well as local dust storms. Such local storms have also been observed by OMEGA. They do not constitute a major factor in mapping the recession of the seasonal cap, as they do not usually travel within the cap itself. The atmosphere remains relatively clear in the visible, in particular in early afternoon, from the southern solstice to the end of the recession ($L_s 325^\circ$) [Wang and Ingersoll, 2002].

[28] High southern latitude regions can only be observed at relatively high incidence angles. The total air mass which has to be crossed by photons on their way from the Sun to the surface, then to the instrument is therefore a critical parameter. The total air mass is presented in Figure 8 for OMEGA observation conditions in late 2004 and 2005. For the south pole itself, the air mass cannot be lower than 3.4 at summer solstice. Therefore air masses of less than 4 can be considered as satisfactory for observations at high southern latitudes. At $L_s 130^\circ$, the local time was optimal (early afternoon, Figure 2b) but the air mass remained high as the Sun was still far to the north. Observation conditions improved at the boundary of the cap until $L_s 210^\circ$, as the recession was slower than the southward motion of the Sun. After $L_s \sim 215^\circ$, the whole seasonal cap could be observed in good solar illumination conditions (total air mass <4). Both the nightside arc (high air mass) and the dayside arc (low air mass) of the orbit could be used from $L_s \sim 220^\circ$ to $L_s \sim 290^\circ$, albeit with different illumination and local time conditions. The dayside arc was closer to the pericenter and it was in the midafternoon to early afternoon for this period (Figure 2e), so that observation conditions were optimum at the highest available spatial resolution.

[29] An example of the impact of aerosols on observed spectra for such observation conditions is presented in Figure 9 for the range of air masses of interest. We selected an observation at $L_s 262^\circ$ of a bright region with strong CO_2 absorption bands, but with a relatively high reflectance in saturated CO_2 bands. This can be considered as a worst case situation for high southern latitudes: the observed region is at 1.2 km above the datum (on the low side for latitudes higher than 75°S and hence on the high side for effective air mass) and the period shortly before southern solstice corresponds to a well defined peak in absorptive cloud activity at high southern latitudes [Neumann *et al.*, 2003]. As expected, aerosol extinction and scattering lower the spectral

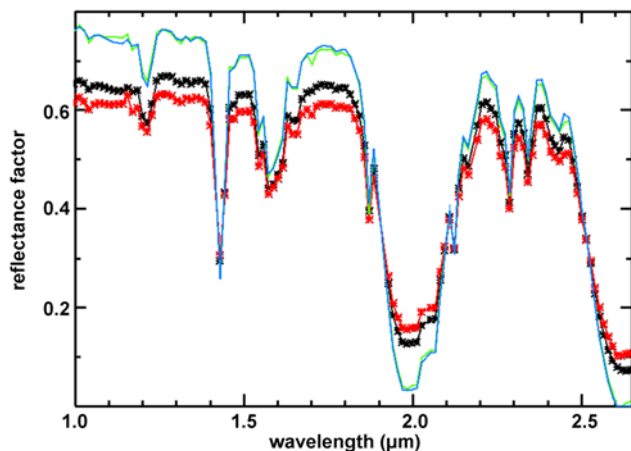


Figure 9. Influence of aerosols on the albedo and band strengths. A region covered by CO₂ ice (316.4°E, 77.6°S) was observed at two incidence angles (red spectrum: 66°; black spectrum: 56.5°) at L_s ~ 263°. These incidence angles correspond to air masses of 3.46 and 2.81, respectively. From the band strengths at 1.435 μm (48.7% and 53.8% for the red and black spectra, respectively), the reflectance factor should be close to 0 above 2.6 μm. The observed reflectance in this range increases with the incidence angle (0.07 at 56.5°, 0.1 at 66°). This is not consistent with a partial coverage by dust within the pixel, supporting the assumption that this contribution results from aerosol scattering. It is then possible to reconstruct the actual surface reflectance spectra from observed spectra by applying the procedure presented by Langevin *et al.* [2006] on the basis of the aerosol model presented by Vincendon *et al.* [2007]. This procedure also provides the optical thickness of aerosols, which is high for the period (0.53 at 1 μm). The closest fits between reconstructed surface spectra (green, blue) are very similar, which validates the aerosol scattering assumption. The retrieved surface reflectance is very low at 2.65 μm, which indicates that there are no ice-free areas within the OMEGA IFOV. The observed reflectance factors at 1.08 μm (0.61 and 0.65 at 66° and 56.5° incidence angles, respectively) are significantly smaller than that derived for the surface itself (0.75). The band depth at 1.435 μm is also significantly reduced, from 66% to 54% (black spectrum) and 49% (red spectrum).

contrast as well as the spatial contrasts. The albedo at 1.08 μm decreases by 13% for an air mass of 2.8 and by 27% for an air mass of 3.45 for such very bright regions. The band strength parameter CO₂(1.435 μm) is reduced by 18% for an air mass of 2.8 and by 27% for an air mass of 3.45. A significant impact of aerosol extinction and scattering on mosaics can be expected whenever there is widespread aerosol activity. It can be seen in some of the mosaics presented in section 4 as a mismatch between overlapping swaths either due to time variations of the aerosol optical thickness (in particular due to streak clouds at L_s 140°–154°) or when a low air mass swath is superimposed on a higher air mass swath (in particular around southern solstice, when both the sunside and nightside arcs could be used; see Figure 3). Even when nadir pointing was

nominal, a few off-nadir tracks with high air mass have been included so as to obtain a more comprehensive coverage, albeit with a significantly lower spatial and spectral contrast due to altitude and aerosol effects. A systematic correction is not straightforward. As discussed by Vincendon *et al.* [2007], it can only be performed on regions which are observed at close intervals with two different observation geometries. Even then, it relies on the assumption that there is no variation of the aerosol optical thickness between the observations. If there is only one geometry of observation, the optical thickness of aerosols can still be determined from the reflectance in saturated CO₂ band, but one has then to assume that there is no dust on the surface of the ice, which is not correct for the dark and cold “cryptic region” [Langevin *et al.*, 2006; Kieffer *et al.*, 2006] and that there are no subpixel areas which are free of ice, which is not the case during the late stages of sublimation [Langevin *et al.*, 2006]. For the vast majority of observations, aerosol effects have a lower impact than that observed at L_s 262°. Therefore we decided as a first step to present the time sequences of mosaics without correcting for aerosol effects. They provide lower limits for the two band depth parameters, CO₂(1.435 μm) and H₂O(1.5 μm), underestimated by a few % up to 30% depending on the optical thickness of aerosols, air mass and altitude, as well as for the albedo of ice covered regions, underestimated by a few % up to 20%. The overall self-consistency of the maps at overlaps between swaths at different incidence angles demonstrates that this approach provides a sound basis for comparing the different stages of the recession of the southern seasonal cap.

[30] Signatures of ices can result either from surface frost or icy aerosols. CO₂ ice is expected to be unstable in the lower atmosphere on the sunlit side [e.g., James *et al.*, 1992]. The optical depth of mesospheric CO₂ ice clouds is very low compared to the path lengths of millimeters to decimeters observed by OMEGA [Clancy and Sandor, 1998; Montmessin *et al.*, 2006]. Therefore the diagnostic CO₂ ice signatures observed by OMEGA can safely be attributed to ice on the surface. The situation is completely different for H₂O ice, as observations in the thermal IR have demonstrated that it is present in aerosols [Smith *et al.*, 2001]. Polar hoods, orographic clouds and aphelion equatorial clouds contain H₂O ice, with grain sizes of a few μm [Clancy *et al.*, 2003]. The predictions of global climate models [Forget *et al.*, 1999; Montmessin *et al.*, 2004] are very consistent with these observations.

[31] The few available observations of the aphelion equatorial belt in the near IR from the ground have reported optical thicknesses of ~0.1 for the 3 μm band [Glenar *et al.*, 2003]. The first comprehensive observations of water-ice rich aerosols in the near IR from orbit were performed by OMEGA in 2004. The maximum strength of the 1.5 μm feature was ~10% for equatorial aphelion clouds [Gondet *et al.*, 2006], which is significantly stronger than expected from the results of Glenar *et al.* [2003]. The relationship between band strength, grain size and optical depth as a function of wavelength is not straightforward, as the optical depth in the near IR sharply decreases if there is an ice-free core due to heterogeneous nucleation [Bell *et al.*, 1996]. The comparison between the maximum ice optical depth of 0.2 observed by TES [Smith *et al.*, 2001] and OMEGA

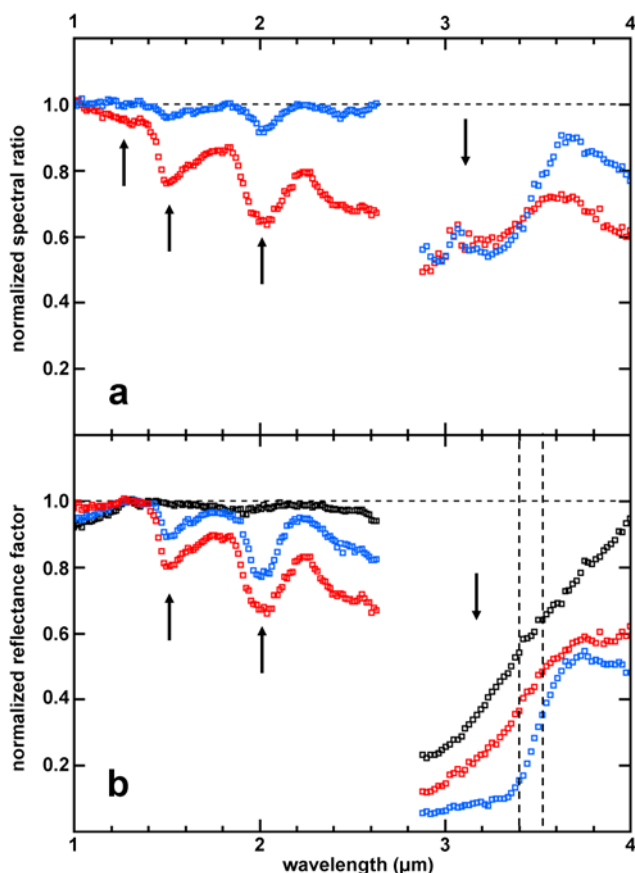


Figure 10. Comparison between spectra of H₂O ice aerosols and surface frosts. In Figure 10a the blue squares correspond to a ratio between the reflectance spectra of a bright terrain (282.8°E, 6.3°N, albedo 0.43) at L_s 85° (weak aphelion cloud: H₂O(1.5 μm) ~3%) and L_s 178.6° (no cloud), normalized to 1 at 1 μm. The red squares correspond to a ratio between the reflectance spectra of the northern slope of a 20-km-sized crater (24.6°E, 27.2°S) at L_s 134° (frost deposit a few km in size) and L_s 173° (after sublimation) normalized to 1 at 1 μm. There are uncertainties on the atmospheric correction at 2 μm, and the air mass is significantly different for the crater slope at 134° (~2.17) and 173° (~3). However, it is clear that the relative strengths of the absorption feature at 3 μm is much enhanced compared to that at 2 μm for H₂O ice in clouds, the 1.5 μm feature being even weaker in relative terms. This is also demonstrated by Figure 10b, which compares the reflectance spectra in a strong equatorial cloud situation normalized to 1 at 1.15 μm (blue squares, L_s 82.7°, 252°E, 12.2°N) and that of the frost deposit of Figure 10a (red squares) to a reference bright spectrum (black squares). The two vertical dashed lines correspond to the wavelength ratio discussed in the text as a discriminator between H₂O ice aerosols and H₂O frost.

observations (10% maximum band strength at 1.5 μm, Figure 10b) for the well documented equatorial aphelion clouds can be used as a benchmark of the relationship of icy aerosol signatures in the thermal IR and near IR. The ice optical depths observed by TES at 12 μm are lower than

0.05 at mid southern latitudes in southern winter (except close to Hellas and Argyre) and at southern high latitudes in southern spring and summer [Smith *et al.*, 2001]. This leads us to the conclusion that H₂O ice band strengths at 1.5 μm for observations at moderate air masses (2 to 4) are expected to be weaker than 10% during this period, while specifically strong signatures are expected in the northern part of Hellas during southern winter from TES results and GCM models [Montmessin *et al.*, 2004]. The contribution from surface H₂O ice is therefore likely to dominate for H₂O ice signatures stronger than 10% at 1.5 μm.

[32] A second criterion takes advantage of the constraints on particle size provided by the relative strengths of unsaturated H₂O ice bands [Grundy and Schmitt, 1998]. H₂O ice grains in the atmosphere are expected to be small: from less than 1 μm to at most 4 μm according to Clancy *et al.* [2003]. Grain sizes for surface H₂O frost range from a few tens of μm to 100 μm from modeling of OMEGA spectra [Schmitt *et al.*, 2005; Langevin *et al.*, 2005]. This difference in grain sizes has a major impact on the shape and relative strength of the absorption bands of H₂O ice at 1.25 μm (only observed for grains larger than ~10 μm), 1.5 μm, 2 μm and 3 μm. In Figure 10, we selected unambiguous examples of surface frost and icy aerosols so as to investigate this relationship. Isolated H₂O ice signatures extending over a few kilometers are relatively common in OMEGA data at latitudes from 25°S to 35°S in mid southern winter. They are located in south facing slopes. Very little ice cloud activity is observed at these latitudes in this season [Clancy *et al.*, 2003]. The case for surface frost is overwhelming, as the spectra can be interpreted from intimate mixing and spatial mixing of local dust with H₂O ice characterized by a 10–100 μm grain size. Such low-latitude frost deposits have recently been reported by Shorghofer and Edgett [2006] by combining visible and thermal IR observations. Examples for ice clouds have been selected with a low incidence angle at latitudes of 5 to 13°N at the northern summer solstice, when no surface frost is expected to survive. As demonstrated by Figure 10a, the 3 μm feature is particularly strong for the small H₂O particles in clouds. This feature saturates for path lengths of a few μm and it is observed in transmission for icy clouds. A multiple scattering situation at the surface of ice-dust mixtures results in a complex interaction of the 3 μm H₂O ice band and the 3 μm hydration band of surface dust, with a lower impact on reflectance in this wavelength range (Figure 10a). The ratio of the features at 2 and 1.5 μm is also a factor of 2 larger for clouds than for surface frost, and the 2 μm band is narrower. Qualitative identification of dominant cloud or frost contributions is therefore relatively straightforward from band shapes. The simplest discrimination criterion is provided by the sharply rising edge of the 3 μm feature in ice cloud signatures between 3.4 μm and 3.525 μm. The additional contribution of thermal emission at 3.525 μm compared to 3.40 μm can be neglected (< 0.02 up to 270 K when converted into reflectance factor units). The ratio between the reflectance factors at these two wavelengths is 0.8 to 0.9 for the 3 μm hydration feature of ice-free aerosols and 0.7 to 0.8 for ice-dust mixtures on the surface compared to ~ 0.4 for aphelion ice-rich clouds (Figure 10b). When CO₂ ice is present, the strong absorp-

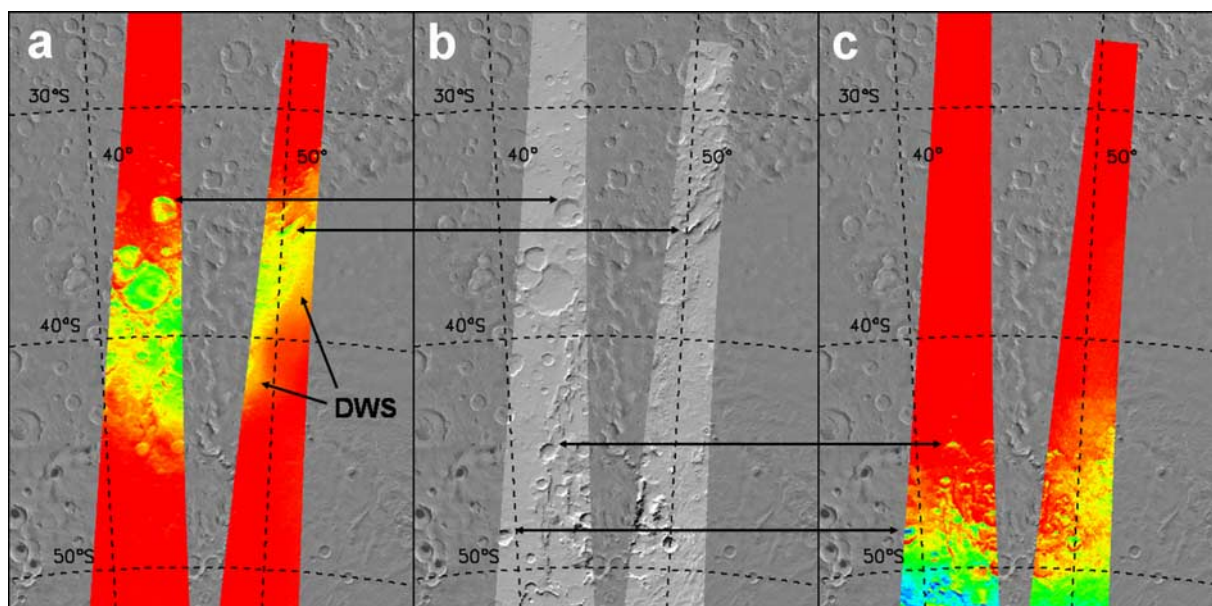


Figure 11. Band depth maps of (a) H_2O at $1.5 \mu\text{m}$ and (c) CO_2 at $1.435 \mu\text{m}$ for the northwest region of Hellas close to the southern winter solstice (track on the right: $L_s 88^\circ$; track on the left: $L_s 94.2^\circ$). The false color table extends from 0% (red) to 60% (dark blue) for H_2O and from 0% (red) to 50% (dark blue) for CO_2 . (b) Within the OMEGA tracks, a shaded relief map based on MOLA elevation is presented with the solar illumination corresponding to OMEGA observations. Surface frosts of (left) H_2O and (right) CO_2 are clearly associated with topography, in particular pole facing slopes (horizontal arrows). Within Hellas, diffuse weak signatures of water ice are observed (labeled DWS in Figure 11a). The relative band strengths correspond to H_2O ice in aerosols. In the northern part of Hellas, such features are observed by TES [Smith *et al.*, 2001] and predicted by models [Montmessin *et al.*, 2004].

tion features in the 1.4 to $3.5 \mu\text{m}$ range prevent directly identifying H_2O ice band shapes. The ratio between the reflectance at $3.4 \mu\text{m}$ and that at $3.525 \mu\text{m}$ ranges from 0.85 to 0.66 for effective grain sizes from a few millimeters to 10 cm ; hence this criterion still provides some handle on icy aerosols over the seasonal cap. A contamination of CO_2 ice by μm -scale H_2O ice grains would have a very similar effect on the $3 \mu\text{m}$ band as H_2O ice in the atmosphere. Such a contamination cannot be excluded, as it could result from heterogeneous nucleation of CO_2 ice on H_2O ice aerosols during southern winter, followed by precipitation. In the following, we will however consider that spectral contributions compatible with μm -scaled H_2O ice aerosols are likely to result from clouds.

[33] Another important discrimination criterion is provided by the link to small-scale topography. For most mid to high southern latitude OMEGA observations, H_2O ice signatures, similarly to CO_2 ice signatures, are preferentially observed on pole-oriented slopes (Figure 11). Such topography linked signatures are observed up to 25°S during southern winter. This behavior is expected for surface frost deposits, while such a close correlation is not consistent with a dominant contribution of H_2O ice signatures from aerosols. Conversely, weak diffuse signatures within Hellas (Figure 11) are confirmed as mainly resulting from H_2O ice aerosols from the strength of the $3 \mu\text{m}$ band, although a small contribution from the surface cannot be excluded.

[34] By combining these approaches (strength of the $1.5 \mu\text{m}$ feature exceeding 10% , slope between $3.4 \mu\text{m}$ and $3.52 \mu\text{m}$, relationship between the $1.5 \mu\text{m}$ and $2 \mu\text{m}$ bands,

link with topography) we concluded that surface H_2O ice represented the dominant contribution for most OMEGA observations of the southern seasonal cap from midspring to the first stages of the formation of the polar hood, shortly between the southern fall equinox. During winter, there is a combination of cloud features to the north of Hellas and surface frost features to the south of the basin. Shortly after equinox, there is clearly a combination of a small but extensive cloud contribution and surface contamination of CO_2 ice by H_2O ice, which will be discussed in section 5 when comparing the H_2O maps with model predictions.

4. Results

[35] The OMEGA observations demonstrate the complexity of the evolution of the south seasonal cap of Mars in terms of composition and physical parameters. The maps of the three selected parameters (Lambert albedo at $1.08 \mu\text{m}$, CO_2 ice absorption strength at $1.435 \mu\text{m}$, H_2O ice absorption strength at $1.5 \mu\text{m}$) are presented for each set of observations from $L_s \sim 90^\circ$ to the end of the recession in Figures 12 to 19. The range of Mars Express orbits and observation conditions (photometric parameters, distance and pixel size) is presented in Table 1 for each set of figures. Discussing every aspect of this very rich data set is beyond the scope of this article. In this section, we therefore focus on a preliminary classification of the regions of the retreating seasonal cap on the basis of their spectral characteristics and on a selected set of comparisons between the

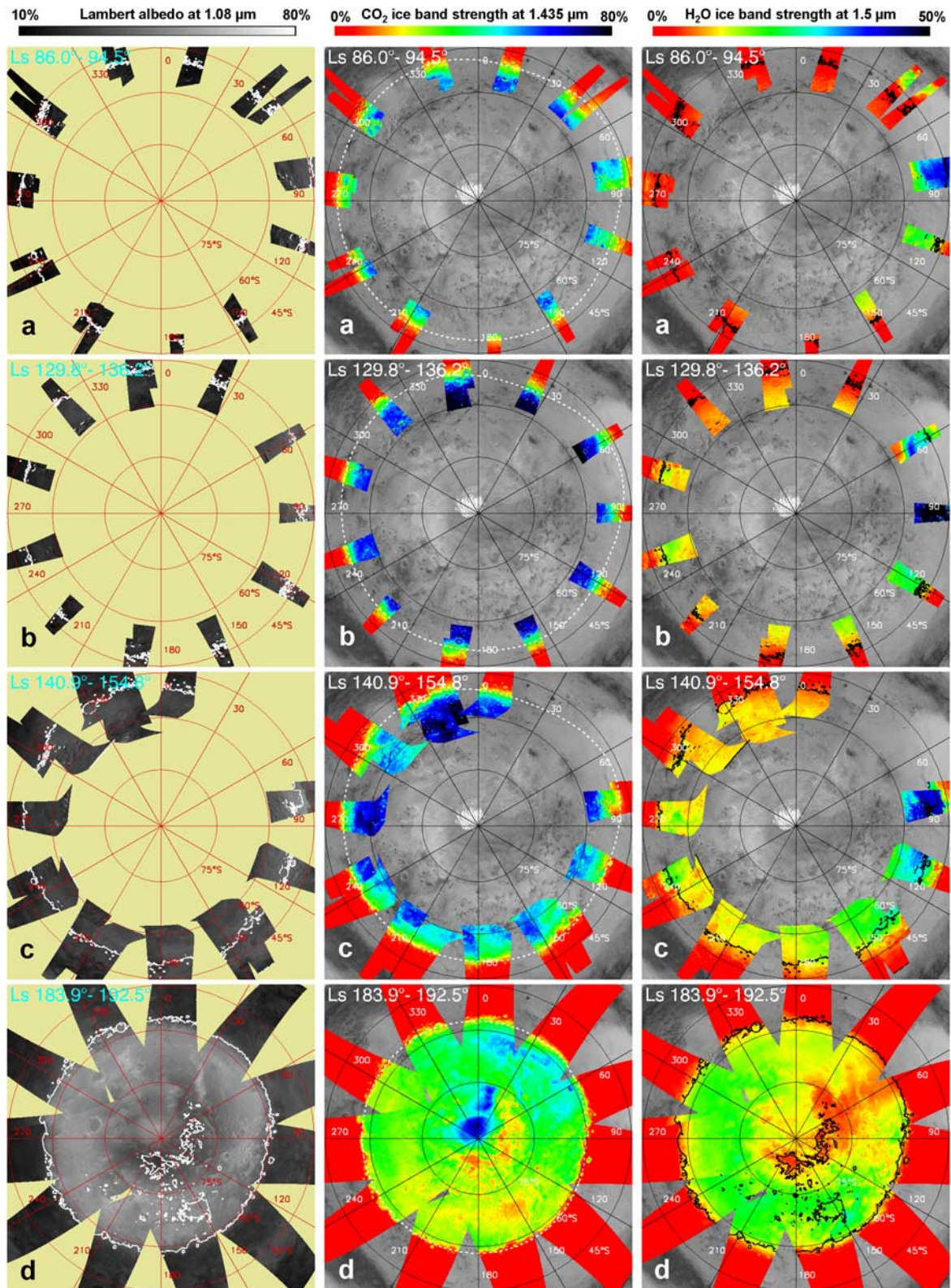


Figure 12. Evolution of the seasonal cap for albedo, CO₂ ice, and H₂O ice signatures for four sets of OMEGA observations from southern winter solstice to shortly after the southern spring equinox. The Figure 12a set was obtained in August 2006; the Figure 12b–12d sets were obtained in late 2004 and early 2005. In the CO₂ ice map, the white dashed line is the cap boundary as observed by TES in late 2000 [Titus, 2005b] for (a) L_s 90°, (b) L_s 133°, (c) L_s 138°, and (d) L_s 180°. The white outline (albedo map) and the black outline (H₂O ice map) correspond to regions exhibiting CO₂ signatures larger than 20% at 1.435 μm.

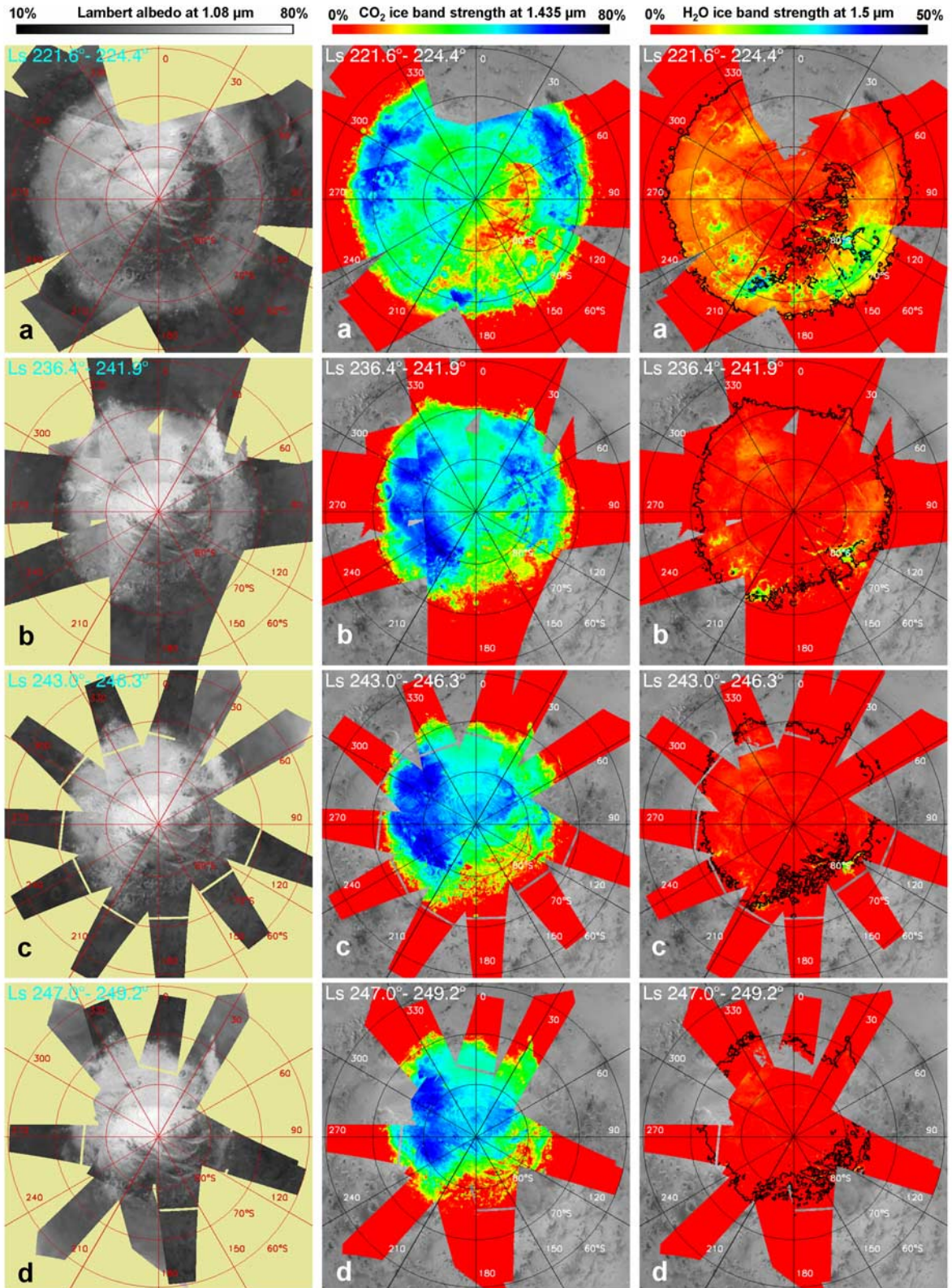


Figure 13. Evolution of the seasonal cap for albedo, CO₂ ice, and H₂O ice signatures for four sets of OMEGA observations: (a) L_s 221.6°–224.4°, (b) L_s 236.4°–241.9°, (c) L_s 243.0°–246.3°, and (d) L_s 247.0°–249.2°. The black outline in the H₂O ice map corresponds to regions exhibiting CO₂ ice signatures larger than 20% at 1.435 μm . Twenty seconds are required for the observation mode of OMEGA. This can result in gaps a few tens of kilometers wide along track (e.g., Figure 13c). The observation conditions and photometric parameters for these four sets of observations are presented in Table 1.

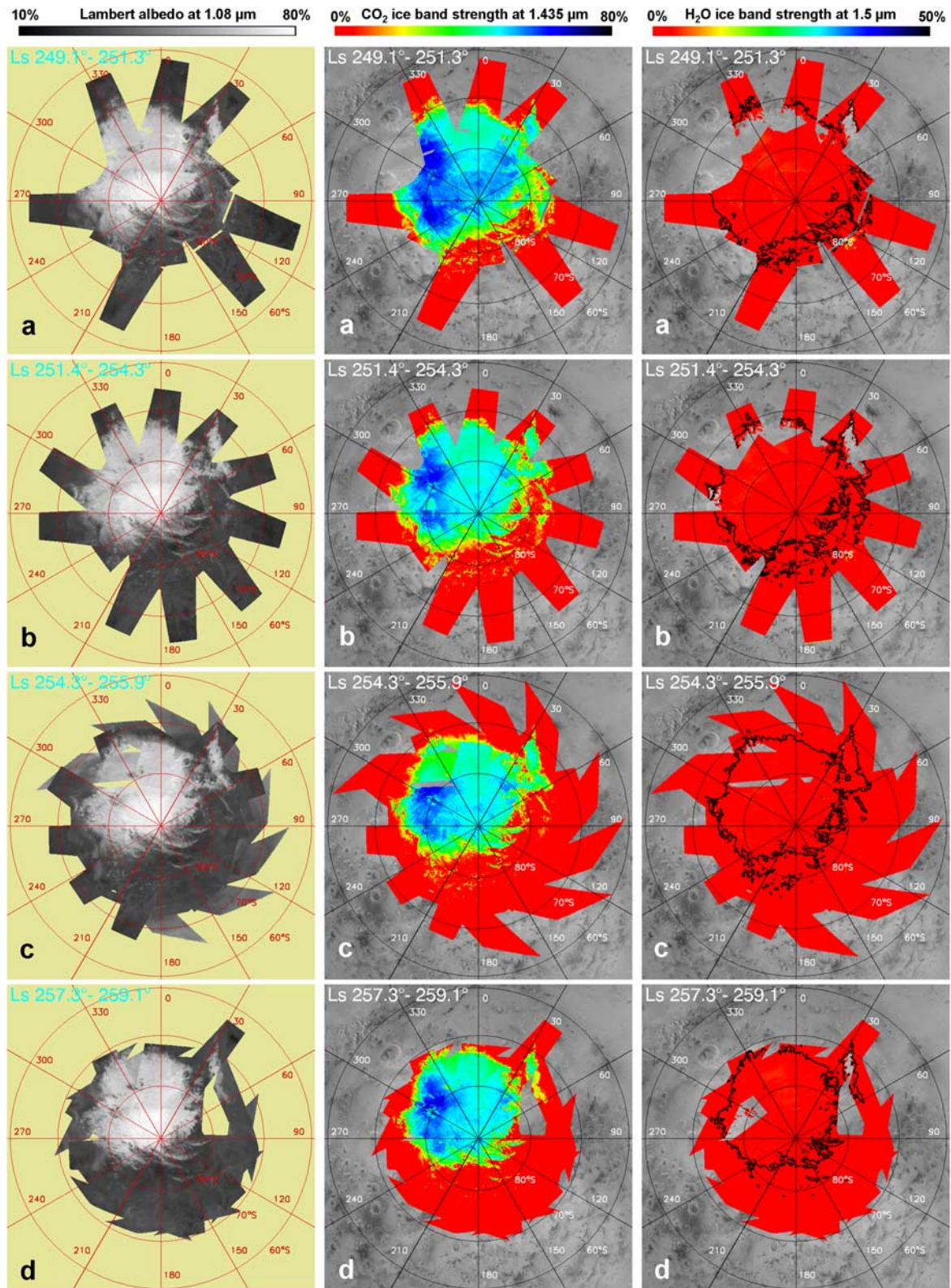


Figure 14. Evolution of the seasonal cap for albedo, CO₂ ice, and H₂O ice signatures for four sets of OMEGA observations: (a) L_s 249.1°–251.3°, (b) L_s 251.4°–254.3°, (c) L_s 254.3°–255.9°, and (d) L_s 257.3°–259.1°. The black outline in the H₂O ice map corresponds to regions exhibiting CO₂ signatures larger than 20% at 1.435 μm . The observation conditions and photometric parameters for these four sets of observations are presented in Table 1.

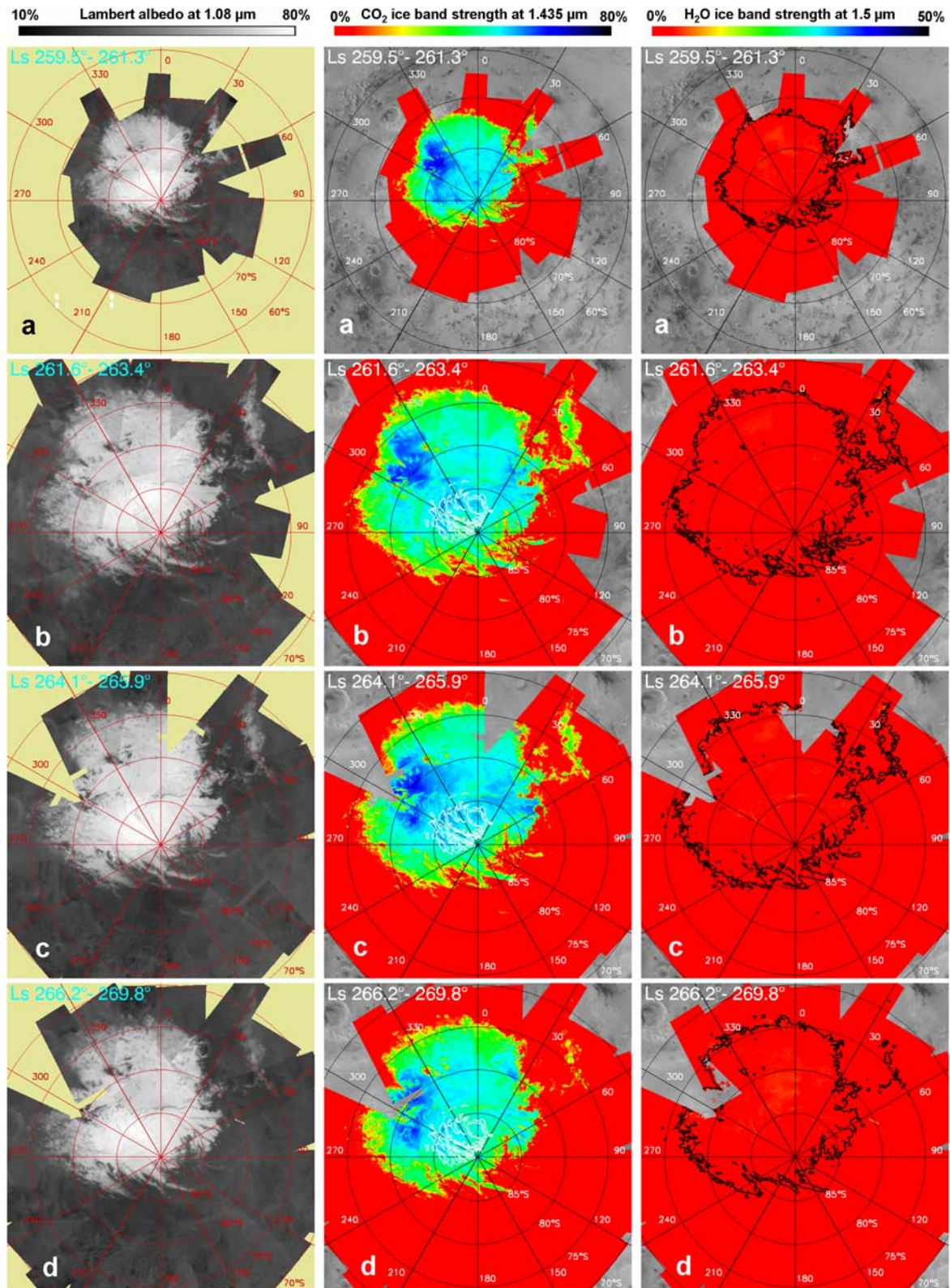


Figure 15. Evolution of the seasonal cap for albedo, CO₂ ice, and H₂O ice signatures for four sets of OMEGA observations: (a) L_s 259.5°–261.3°, (b) L_s 261.6°–263.4°, (c) L_s 264.1°–265.9°, and (d) L_s 266.2°–269.8°. The black outline in the H₂O ice map corresponds to regions exhibiting CO₂ signatures larger than 20% at 1.435 μm . The white outline in the CO₂ ice map corresponds to the boundary of the perennial cap. The observation conditions and photometric parameters for these four sets of observations are presented in Table 1.

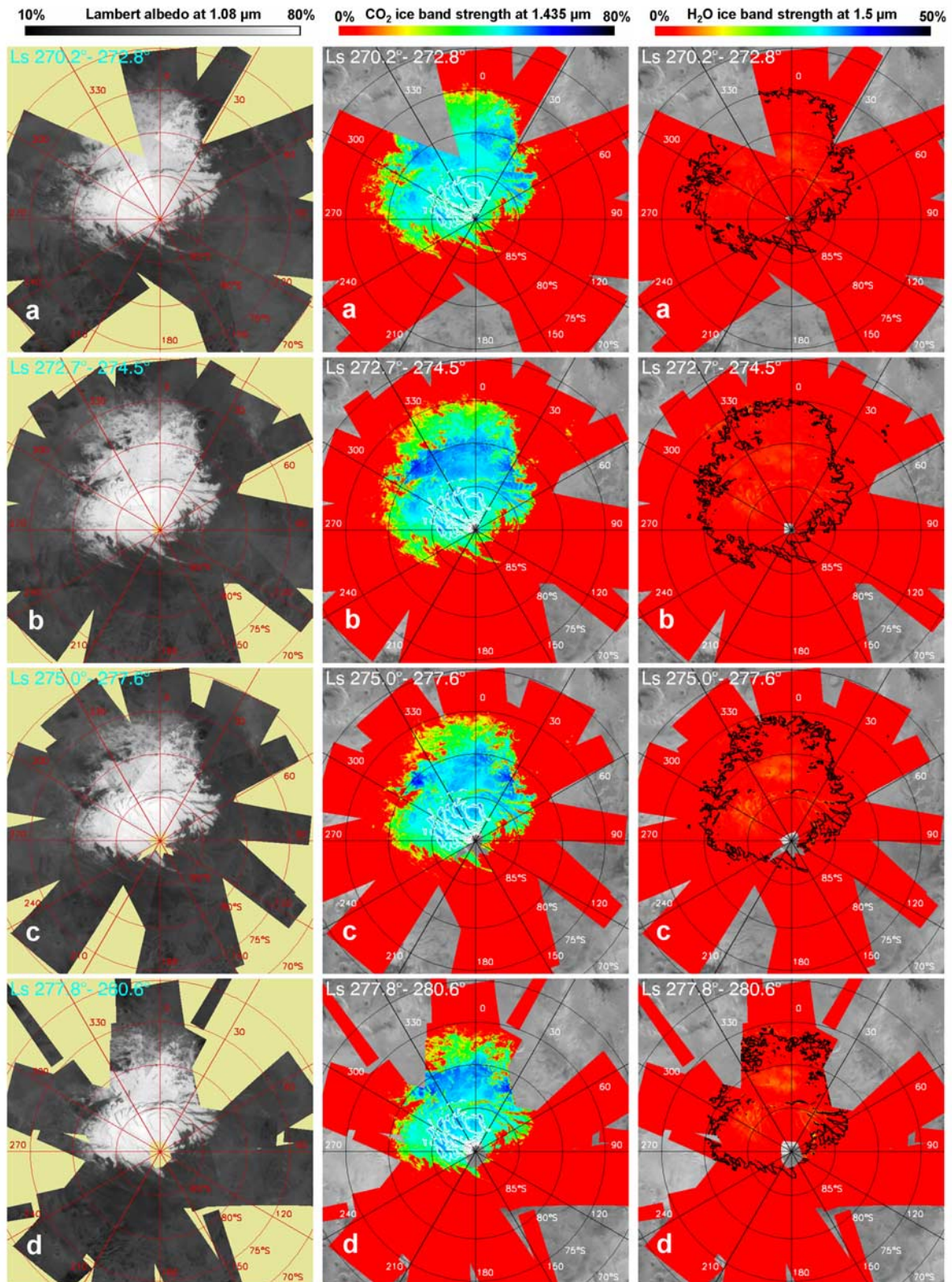


Figure 16. Evolution of the seasonal cap for albedo, CO₂ ice, and H₂O ice signatures for four sets of OMEGA observations: (a) L_s 270.2°–272.8°, (b) L_s 272.8°–274.5°, (c) L_s 275.0°–277.6°, and (d) L_s 277.8°–280.6°. The black outline in the H₂O ice map corresponds to regions exhibiting CO₂ signatures larger than 20% at 1.435 μm . The white outline in the CO₂ ice map corresponds to the boundary of the perennial cap. The observation conditions and photometric parameters for these four sets of observations are presented in Table 1.

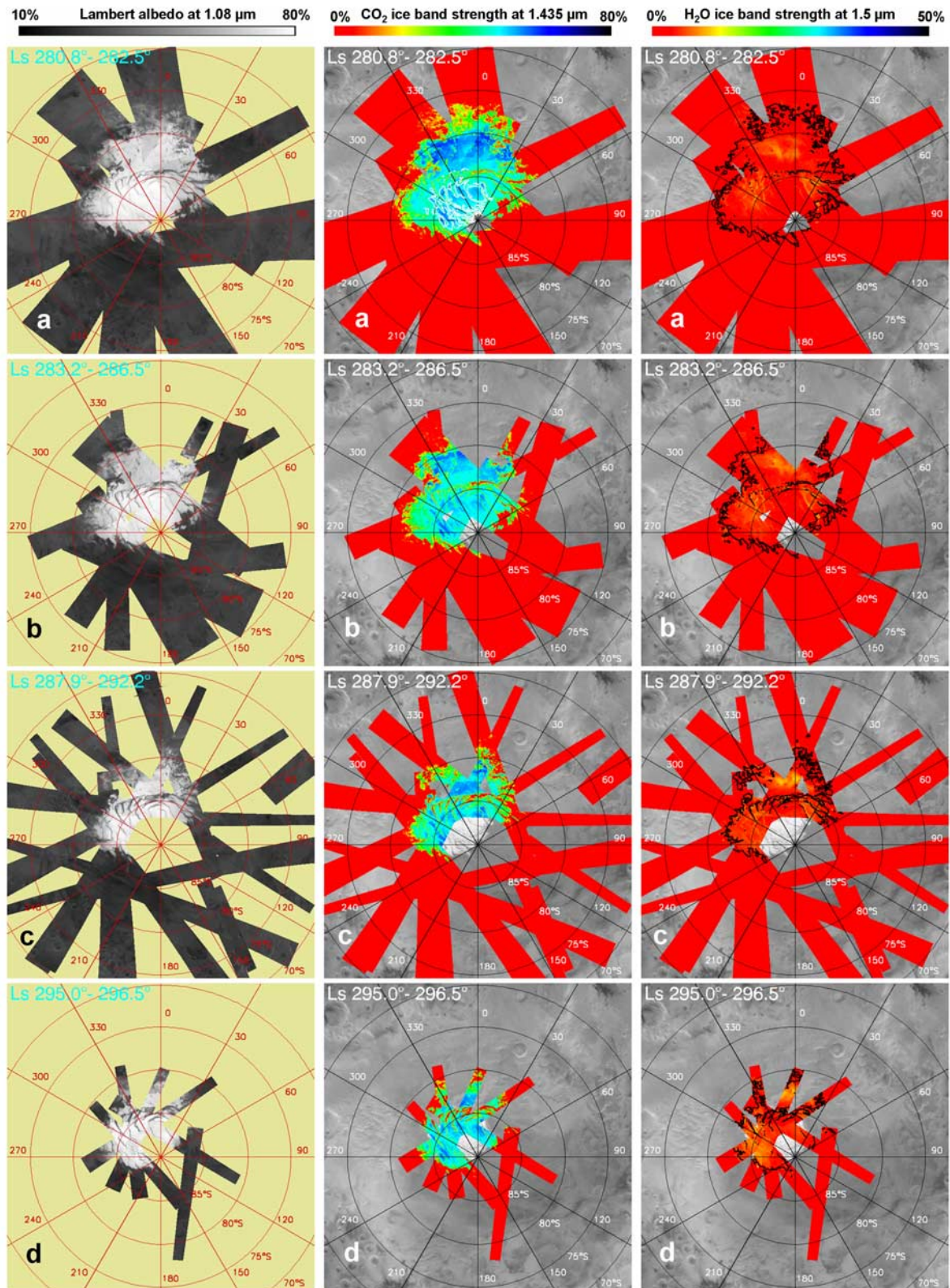


Figure 17. Evolution of the seasonal cap for albedo, CO₂ ice, and H₂O ice signatures for four sets of OMEGA observations: (a) L_s 280.8°–282.5°, (b) L_s 283.2°–286.5°, (c) L_s 287.9°–292.2°, and (d) L_s 295.0°–296.5°. The black outline in the H₂O ice map corresponds to regions exhibiting CO₂ signatures larger than 20% at 1.435 μm . The white outline in the CO₂ ice map corresponds to the boundary of the perennial cap. The observation conditions and photometric parameters for these four sets of observations are presented in Table 1.

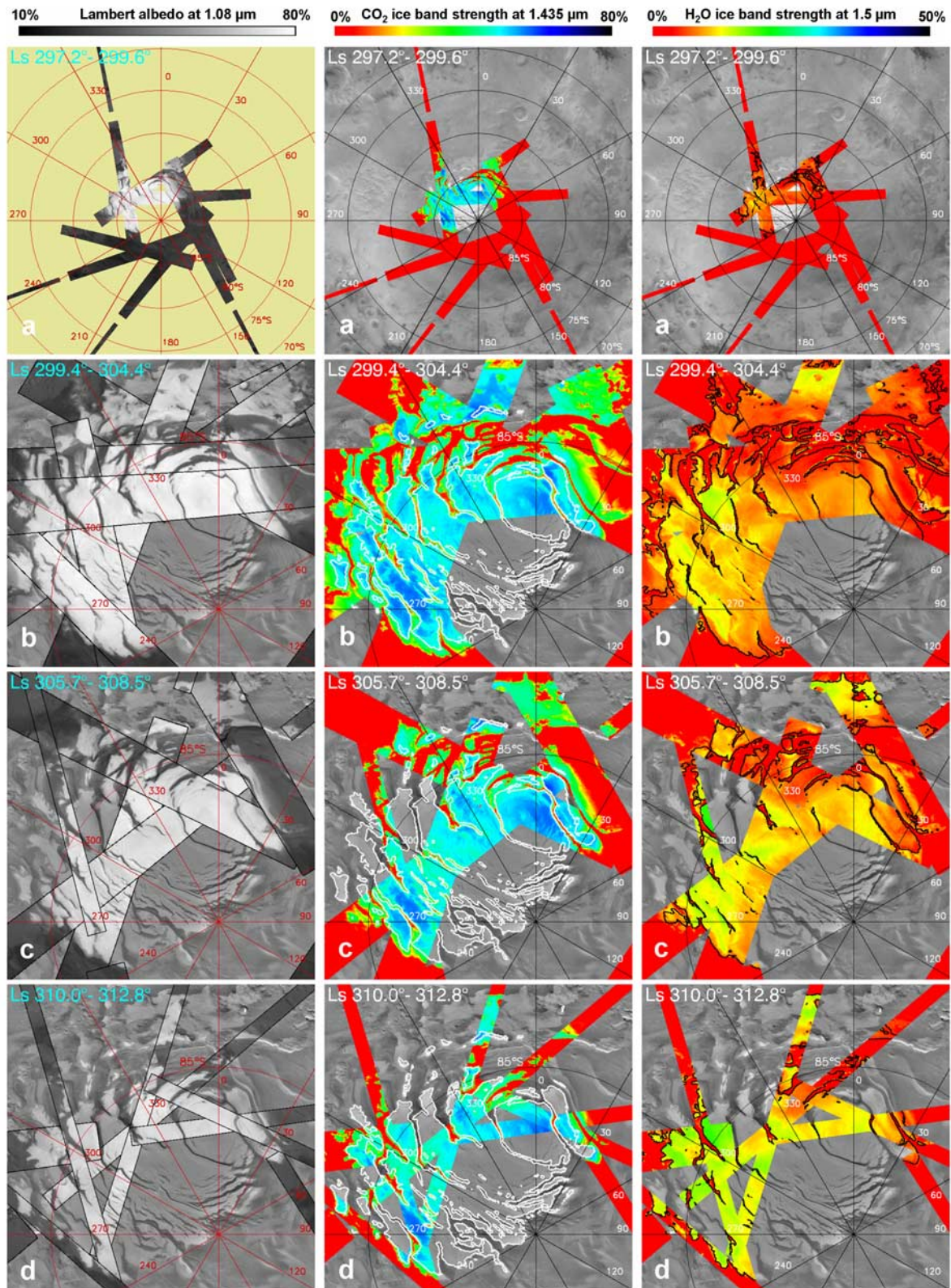


Figure 18. Evolution of the seasonal cap for albedo, CO₂ ice, and H₂O ice signatures for four sets of OMEGA observations: (a) L_s 297.2°–299.6°, (b) L_s 299.4°–304.4°, (c) L_s 305.7°–308.5°, and (d) L_s 310.0°–312.8°. The black outline in the H₂O ice map corresponds to regions exhibiting CO₂ signatures larger than 20% at 1.435 μm . The white outline corresponds to the boundary of the perennial cap (from the albedo in Viking HR mosaics, USGS/NASA, underlying the maps). The observation conditions and photometric parameters for these four sets of observations are presented in Table 1.

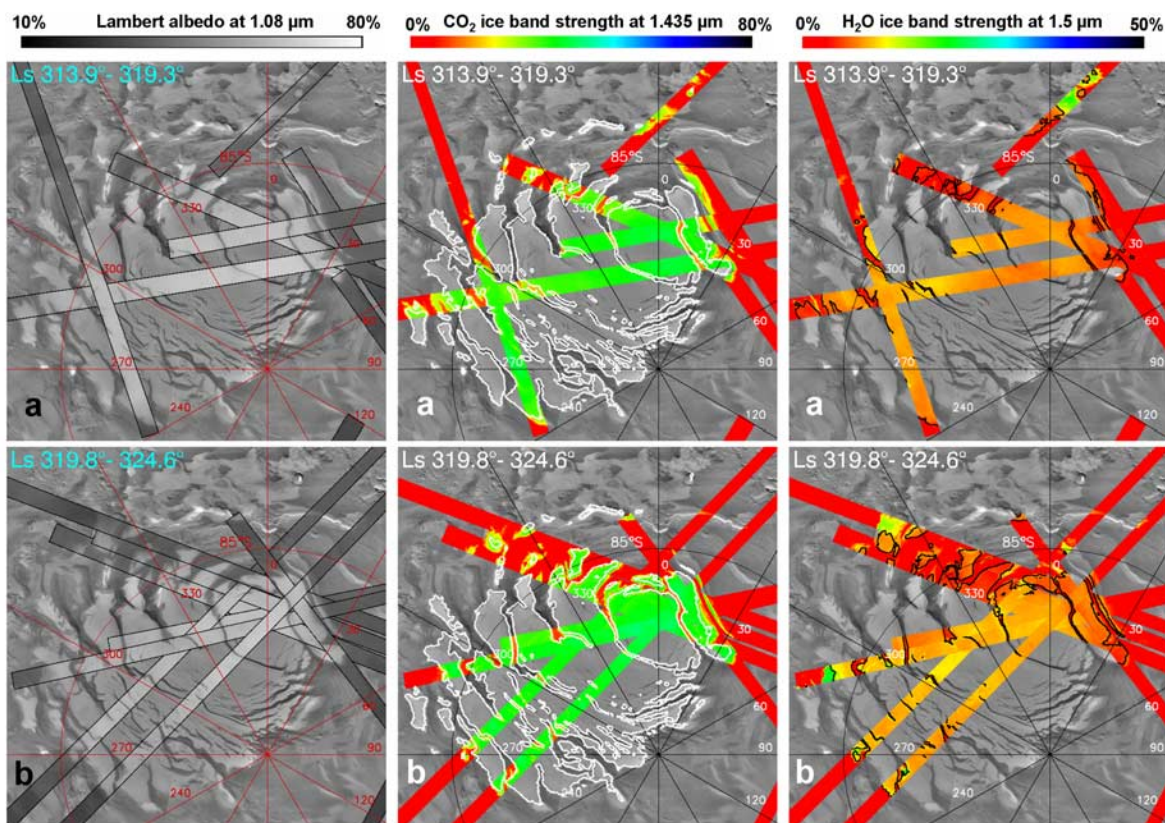


Figure 19. Evolution of the seasonal cap for albedo, CO₂ ice, and H₂O ice signatures in the very last stages of the recession for two sets of OMEGA observations: (a) L_s 313.9°–319.3° and (b) L_s 319.8°–324.6°. The black outline in the H₂O ice map corresponds to regions exhibiting CO₂ signatures larger than 20% at 1.435 μm. The white outline corresponds to the boundary of the perennial cap (from the albedo in Viking HR mosaics, USGS/NASA, underlying the maps). At these very late stages of the recession, the areas covered by a mixture of H₂O ice and dust which have been reported by *Bibring et al.* [2004a] are observed at the same locations. The observation conditions and photometric parameters for these two sets of observations are presented in Table 1.

OMEGA observations and previous observations of the seasonal cap.

4.1. Spectral Classification and Spectral Evolution

[36] Figure 20 showcases the remarkable spectral diversity of the southern seasonal cap. The heliocentric longitude and location of each observation is presented in Table 2. The spectral modeling methods which are implemented are derived from the approaches of *Douté and Schmitt* [1998] and *Poulet et al.* [2002]. The spectral evolution of southern seasonal cap regions is more complex than that observed in the north seasonal cap. A typical area of the north seasonal cap starts as CO₂ ice contaminated by small-grained H₂O ice and dust, then the CO₂ ice contribution decreases, and finally the area moves along the mixing line between H₂O frost and dust until sublimation is complete [*Schmitt et al.*, 2005]. The spectra from the south seasonal cap show that CO₂ ice is the dominant constituent in terms of volume fraction, which is expected as there is very little available H₂O in the atmosphere, at most a few tens of precipitable μm [*Houben et al.*, 1997; *Montmessin et al.*, 2004]. However, the range of average path lengths within CO₂ ice (from a

few millimeters to several tens of centimeters), H₂O and dust contamination levels is much wider than in the north seasonal cap. Three major spectral classes can be identified from the relative level of CO₂ ice and H₂O ice signatures.

[37] Spectral class I corresponds to spectra dominated by CO₂ ice signatures. It can be decomposed into 4 spectral subclasses:

[38] I.a: This class is characterized by strongly saturated spectral signatures of CO₂ associated with a low Lambert albedo (albedo: dark grey; CO₂: dark blue; H₂O: orange to red). Modeling such spectra requires path lengths of several tens of centimeters [*Langevin et al.*, 2006]; hence this class is interpreted as a clean slab 20 cm to 50 cm thick of CO₂ ice overlying the original surface. It is observed over a wide range of longitudes during southern winter (Figures 12a to 11c). In such regions, there is no well defined albedo contrast at the edge of the seasonal cap. If the interface has a low roughness, slab ice can even lower the albedo when compared to the bare surface due to specular reflection. Immediately after sunrise at the pole, slab ice spectra are observed over an area closely corresponding to the outlines of the perennial cap (Figure 12d) with a higher

Table 1. Range of Heliocentric Longitudes, Photometric Parameters, and Pixel Sizes for the OMEGA Observations Reported in Figures 12–19^a

Figure	Mex Orbits		M-Year	Ls, deg		Target Lat.	Local Time, h		Inci., deg		Emer., deg		Distance, km		IFOV, km	
12a	3283	3347	28	86.4	94.3	50°S	13.5	14.3	78	81	0	4	2390	3120	3.0	3.9
12b	1170	1216	27	129.9	136.1	50°S	13.5	14.1	71	75	0	4	1650	2030	2.1	2.5
12c	1251	1348	27	141.0	154.8	50°S	12.2	13.4	61	68	0	6	2370	3560	3.0	4.5
12d	1539	1592	27	183.9	192.5	75°S	9.0	10.8	70	76	44	46	7120	8170	8.9	10.2
13a	1765	1774	27	221.7	223.2	75°S	8.6	17.9	65	75	5	23	5420	6850	6.8	8.6
13b	1849	1880	27	236.4	241.9	75°S	7.1	16.8	63	66	0	24	3380	5280	4.2	6.6
13c	1887	1903	27	243.2	246.0	75°S	16.2	16.8	62	64	0	6	3050	3280	3.8	4.1
13d	1909	1921	27	247.1	249.2	75°S	8.1	17.2	58	65	0	11	2830	5100	3.5	6.4
14a	1921	1933	27	249.2	251.3	75°S	7.7	16.2	59	61	0	11	2730	5050	3.4	6.3
14b	1934	1947	27	251.5	253.8	75°S	7.0	16.3	58	64	0	10	2530	4910	3.2	6.1
14c	1950	1958	27	254.3	255.8	75°S	4.3	15.9	58	73	0	9	2340	4740	2.9	5.9
14d	1967	1976	27	257.4	259.0	75°S	5.4	15.6	57	69	0	4	2270	4500	2.8	5.6
15a	1979	1989	27	259.5	261.3	75°S	5.1	15.4	56	70	0	3	2120	4310	2.7	5.4
15b	1991	2001	27	261.6	263.4	75°S	5.0	15.8	54	70	0	6	2000	4110	2.5	5.1
15c	2005	2015	27	264.1	265.9	75°S	4.7	15.3	55	71	0	2	1880	3890	2.4	4.9
15d	2017	2037	27	266.2	269.8	75°S	4.4	14.9	53	72	0	3	1720	3700	2.2	4.6
16a	2041	2054	27	270.5	272.8	75°S	4.1	14.6	53	72	0	5	1570	3360	2.0	4.2
16b	2054	2064	27	272.7	274.5	75°S	3.9	14.4	53	73	0	9	1500	3190	1.9	4.0
16c	2067	2081	27	275.0	277.5	75°S	3.4	14.1	52	75	0	7	1390	3040	1.7	3.8
16d	2083	2099	27	277.8	280.6	75°S	3.6	14.0	51	74	0	7	1270	2820	1.6	3.5
17a	2100	2110	27	280.8	282.5	75°S	3.3	13.8	52	75	0	3	1210	2640	1.5	3.3
17b	2114	2133	27	283.2	286.5	75°S	2.6	13.9	52	78	0	7	1080	2480	1.4	3.1
17c	2141	2165	27	287.9	292.0	75°S	2.6	13.3	52	79	0	7	920	2160	1.2	2.7
17d	2183	2191	27	295.0	296.4	85°S	2.7	12.0	63	71	0	8	1050	1400	1.3	1.8
18a	2196	2210	27	297.2	299.6	85°S	2.3	11.0	63	72	0	7	1000	1340	1.3	1.7
18b	2209	2239	27	299.4	304.4	85°S	3.1	10.5	64	73	0	10	880	1190	1.1	1.5
18c	2247	2262	27	305.7	308.2	85°S	3.0	10.1	66	74	0	5	770	1020	1.0	1.3
18d	2274	2290	27	310.2	312.8	85°S	2.9	10.0	67	76	0	4	660	870	0.8	1.1
19a	2297	2330	27	313.9	319.2	85°S	1.8	10.0	68	77	0	6	530	790	0.7	1.0
19b	2334	2364	27	319.8	324.6	85°S	1.0	9.5	71	81	0	10	450	660	0.6	0.8

^aAll observations have been performed during Martian year 27 (5 March 2004 to 21 February 2006) except for that reported in Figure 12a, performed in August 2006 during Martian year 28. The range of photometric parameters of each set of observations is reported for a latitude which is representative of that of sunlit regions of the cap at the time of observation (50°S in early to mid southern winter, 75°S in southern spring and early southern summer, 85°S in late southern summer). In spring and early summer (L_s 222° to L_s 300°), the orbit plane moves toward the noon-midnight plane, so that the difference in incidence angle at 75°S latitude between the nightside and the dayside of the orbit increases. Emergence angles are low except for Figure 12d, so that the phase angle is in general similar to the incidence angle; hence it is not indicated.

albedo as the underlying surface is the relatively bright perennial cap.

[39] I.b: such spectra have a very high albedo (~ 0.7 , probably close to 0.8 for the surface itself) associated with strong CO₂ absorption features (albedo: very light grey; CO₂: blue; H₂O: red). The band strength at 1.435 μm , the partially saturated 2 μm , the absorption edge at 2.55 μm and the shape of the 3.3 μm band all indicate path lengths in the range of ~ 10 cm, corresponding to a mean distance between scattering interfaces within the CO₂ ice (“equivalent grain size” from grain boundaries, fractures, scattering inclusions. . .) of ~ 5 cm. The latter spectra are typical of the “bright cap” [Kieffer *et al.*, 2000] and more generally outer regions of the seasonal cap during spring and early summer.

[40] I.c: These spectra are extremely bright (albedo ~ 0.8 before aerosol correction) with significantly weaker absorption features than type I.b spectra (albedo: white; CO₂: green; H₂O: red). The band strength at 1.435 μm , the band shape at 2 μm , the absorption edge at 2.6 μm and the shape of the band at 3.3 μm require equivalent grain sizes of a few mm. They are observed in the central part of the seasonal cap (in particular over high-altitude areas such as that corresponding to the perennial cap) from midspring (Figure 13a) to late summer (Figure 18c). Subclasses I.a, I.b

and I.c correspond to remarkably clean CO₂ ice: an upper limit of a few tens of ppm can be set on the volume fraction of dust and H₂O ice inclusions in a granular mixture.

[41] I.d: Such spectra have a low albedo and weak absorption features (albedo: dark grey; CO₂: orange; H₂O: red). They are typical of the “cryptic region” as defined by Kieffer *et al.* [2000] in midspring (Figure 13a). The brightness temperature at 5.1 μm is very low (< 190 K) which precludes significant subpixel contributions of ice free areas (Figure 21). The cryptic region is extensively discussed by Langevin *et al.* [2006]. Extensive dust contamination of the upper layers of a thick slab of CO₂ ice is required to interpret the spectral evolution of these areas. Part of this dust may be brought to the surface by a venting process as suggested by Kieffer *et al.* [2006]. Two different types of I.d spectra are observed (Figure 21): that of the cryptic region (dark and cold) and that of regions close to the sublimation front. Such spectra present CO₂ ice signatures which are very similar to that in the cryptic region, but the brightness temperature at 5.1 μm is now high. They can be adequately modeled by subpixel mixing between areas still covered with CO₂ ice (red and green spectra in Figure 20a) and a dominant ice free component at temperatures of 235–245 K (Figure 21), which are very consistent with that measured for ice-free regions at high southern latitudes in

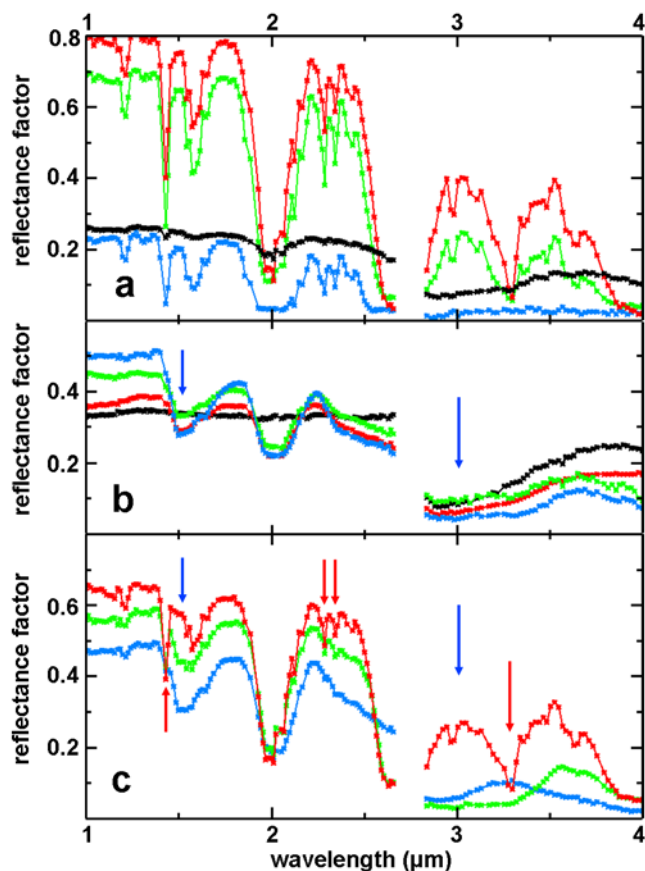


Figure 20. Spectral diversity during the recession of the southern seasonal cap. The location and time of each observation are indicated in Table 2. (a) Most areas are dominated by CO₂ ice. The mean path length within CO₂ ice is strongly constrained by the strength of the 1.435 μm band and the shape of the 3.3 μm band. (b) A few areas are spectrally dominated by H₂O ice. This is the case close to Hellas in early to mid southern winter (blue spectrum). Only a few patches survive until midspring (red spectrum). One had to wait until the very end of the recession (L_s 325°) to observe H₂O ice patches at the boundary of the permanent cap, confirming the findings of *Bibring et al.* [2004a]. (c) Some areas exhibit both the CO₂ and H₂O ice signatures. Areas spectrally dominated by H₂O ice within the cap (blue) still present evidence for CO₂ ice. The seasonal cap right after equinox is significantly contaminated by H₂O ice crystals, and there are a few μm-pr of H₂O ice in the atmosphere (green). There is also a minor H₂O ice contamination for regions corresponding to the perennial cap at L_s 325° (red). The classification derived from these spectra is reported in the text and in Table 2, together with the time and location of each observation.

the thermal IR [*Paige and Keegan*, 1994]. Therefore one can refer to such spectra as “non-cryptic” weak CO₂ ice signatures. Contrary to the north seasonal cap, where no direct transition from CO₂ ice to dust is observed [*Schmitt et al.*, 2005], spectra of this type are observed for the whole range of mixing ratios between subpixel areas covered by CO₂ ice and dust when crossing the sublimation front.

[42] Class II spectra are characterized by moderate to high albedos and the presence of both CO₂ ice and H₂O ice absorption features (albedo: light grey to very light grey; CO₂: green to orange; H₂O: blue to orange). Subclasses (a, b, c) can be defined from the relative strength of the CO₂ and H₂O ice features (see Table 2). The drastic impact of the 3 μm H₂O band (blue arrow) on the 3.3 μm band (red arrow) is demonstrated in Figure 20c. This is in particular the case for ice-rich clouds (section 3.4). As discussed by *Bibring et al.* [2004a] and *Schmitt et al.* [2005], spectra dominated by H₂O ice features can be obtained with less than 1000 ppm of H₂O ice (grain size: a few tens of μm to 100 μm, similar to H₂O frost) embedded in CO₂ ice. The albedo is mainly controlled by the amount of dust within or at the surface of the ice. Scattering on dust and H₂O ice inclusions limits the path length of photons in CO₂ ice. There is only a lower limit constraint of a few hundred μm on the distance between interfaces in the CO₂ ice itself, as it must be much larger than the size of inclusions. Regions of the seasonal cap presenting H₂O ice signatures are very extended shortly after the southern spring equinox (Figure 12d) and at the very end of the recession (Figures 18c and 18d). As discussed in section 3.4, ice-rich clouds significantly contribute after the equinox, in particular for the 3 μm feature. This will be further discussed when comparing the maps of H₂O signatures with the predictions of circulation models in section 5.

[43] Class III spectra present only signatures of H₂O ice. The observed albedo of such areas is always lower than 0.5 at southern latitudes (albedo: gray, CO₂: red, H₂O: yellow to blue). The deepest signatures are observed in the southern parts of Hellas during winter (Figures 11a, 11b, and 11c). A few isolated regions dominated by H₂O ice survive until late spring (Figure 15a). These spectra can all be interpreted as small-grained H₂O ice on the surface (a few tens of μm to 100 μm) with different levels of dust contamination, an ice-free terrain (black spectrum in Figure 20d) constituting a satisfactory end-member for the sequence of class III spectra. The H₂O ice to dust sequence as observed in the south seasonal cap closely resembles that observed in the north seasonal cap.

[44] For any region of interest, it is possible to obtain the sequence of spectra as a function of time. The frequency of coverage increases for higher latitudes. A first example was given with the evolution of the cryptic region by *Langevin et al.* [2006]. Here we present two other examples: a region on the perennial cap (299°E, 87°S) and the region at 34°E, 76°S which presented a spectrum of type I.d with a thermal contribution from ice free regions at L_s 262° in Figure 21. Shortly after equinox, the perennial cap (Figure 22) exhibits a relatively bright spectrum of type I.a (slab ice). There is a major contribution of aerosols in the continuum of saturated bands (2 μm, 2.7 μm), which is not surprising as the incidence angle is extremely high (86°, total air mass 15). Aerosol scattering also dominates from 2.8 to 3.6 μm, as the reflectance of a slab of CO₂ ice is very small in this spectral region. In midspring (L_s 223°), the albedo has increased and the grain size has decreased to a few mm. This spectrum, which corresponds to the red spectrum in Figure 20a, stays stable until a few weeks after summer solstice, then the albedo starts to decrease again. There is a peak in H₂O ice

Table 2. Timing, Location, Albedo, and Spectral Signatures of Representative Spectra From Figure 20

Class	Figure 20	L_s	Longitude	Latitude	Albedo (1.08 μm)	CO_2 (1.435 μm)	H_2O (1.5 μm)
I.a	a (blue)	142°	344°E	60°S	0.23	0.81	0.11
I.b	a (green)	261°	302°E	78°S	0.68	0.64	0.03
I.c	a (red)	273°	299°E	87°S	0.79	0.46	0.03
I.d	a (black)	223°	80°E	82°S	0.25	0.08	0.02
II.a	c (red)	325°	355°E	87°S	0.64	0.37	0.10
II.b	c (green)	187°	300°E	65°S	0.56	0.24	0.24
II.c	c (blue)	224°	200°E	73°S	0.47	0.10	0.36
III	b (blue)	138°	85°E	47°S	0.50	0.03	0.43
III	b (green)	325°	280°E	83°S	0.45	0.00	0.24
III	b (red)	250°	135°E	77°S	0.36	0.00	0.23
Reference	b (black)	325°	60°E	70°S	0.33	0.00	0.00

contamination at L_s 311° (type II). This is not due to an icy cloud as the impact on the 3 μm band is not as severe as it should be considering the strength of the 1.5 μm H_2O absorption. The final spectrum (L_s 313°) is very similar to that observed on the perennial cap at L_s 345° in January 2004. As discussed by *Bibring et al.* [2004a] and *Douté et al.* [2007] some dust contamination is required to explain the lower albedo. The initial and final albedos in the continuum are similar, but the spectral shapes are completely different, with a thick transparent slab of CO_2 ice overlying the perennial cap at L_s 187°, then breaking up (possibly due to thermal stresses as the Sun rises over the pole), and CO_2 ice contaminated by dust and H_2O ice at L_s 313° to L_s 345°.

[45] The region at 34°E, 76°S is representative of many outer regions of the cap. Immediately after equinox (black spectrum in Figure 23), the region is covered by an ice-rich cloud, which results in an absorption of $\sim 5\%$ at 1.5 μm and a much larger reduction of the reflectance at 3 μm . From L_s 223° to L_s 255°, there is no signature of an ice cloud. The albedo increases up to 60% (L_s 240°), then decreases to 50% while keeping a grain size in the range of 10 μm . After L_s 255°, the decrease of the albedo is linked to an increasing contribution from ice-free areas at a subpixel scale as presented in Figure 21 (reduction in spectral contrast, decrease of the 3 μm reflectance due to the hydration band in Martian terrains, increase in temperature). At L_s 265°, there is still a small but unmistakable CO_2 ice signature. Therefore 15 days separate the apparition of the first ice-free subpixel patches from the sublimation of the last CO_2 ice patch within an IFOV of 2×2 km, which is consistent with the 20 days temperature rise period observed by TES at the edge of the retreating cap [*Kieffer et al.*, 2000]. Apart from the thin icy cloud cover after equinox, no signature of H_2O is observed until the end of sublimation. The last three spectra are nearly superimposed over a period of nearly one month, which is consistent with a relatively clear atmosphere after the southern summer solstice in early afternoon [*Wang and Ingersoll*, 2002].

[46] Long-term evolutions are observed for the long wavelength IR channel (above 2.7 μm in Figure 20) with decreases of up to 20% of the photometric efficiency, as discussed by *Jouglet et al.* [2007]. Therefore the reflectance factor above 2.7 μm may be underestimated with respect to that at shorter wavelengths. However, the impact on relative values of the reflectance factor within a given spectrum is in

the range of a few %; hence the evolution of the shape of spectral signatures observed in this spectral range is reliable.

4.2. Spatial Distribution of Bright Regions and CO_2 Ice Signatures: Comparison With Previous Observations of the Seasonal Cap

[47] In southern winter (Figures 12a, 12b, and 12c), the seasonal cap shows very little albedo contrast at the boundary of the CO_2 ice signatures. Significant albedo features are linked to extensive dust cloud activity, which is well documented for this range of L_s [*Wang and Ingersoll*, 2002; *Smith et al.*, 2003; *Neumann et al.*, 2003] and H_2O ice contamination both in clouds (northern half of Hellas)

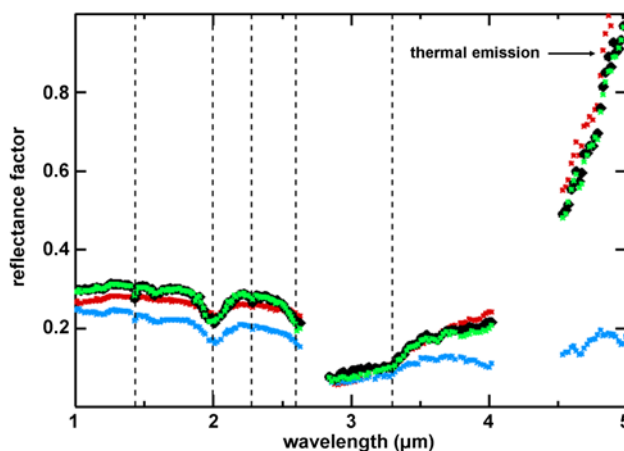


Figure 21. Two examples of spectra with weak CO_2 ice features (spectral subclass I.d). The blue spectrum corresponds to the cryptic region (L_s 223°, 80°E, 82°S). No thermal emission is observed, which requires $T < 190$ K. The green spectrum is observed at 34°E, 76°S close to the sublimation front at L_s 262°. It presents very similar spectral characteristics up to 3 μm , but a strong thermal emission contribution is observed. This spectrum is very adequately modeled (underlying black spectrum) by a subpixel areal mixture with 10% bright CO_2 ice (red spectrum from Figure 20a) and 90% ice-free areas (red spectrum, nearby ice-free region) with an apparent temperature of 238 K (assuming an emissivity of 0.85 at 5 μm). A larger-grained CO_2 ice component (green spectrum from Figure 20a) also provides a reasonable fit with a slightly larger fraction of ice-covered areas (13%).

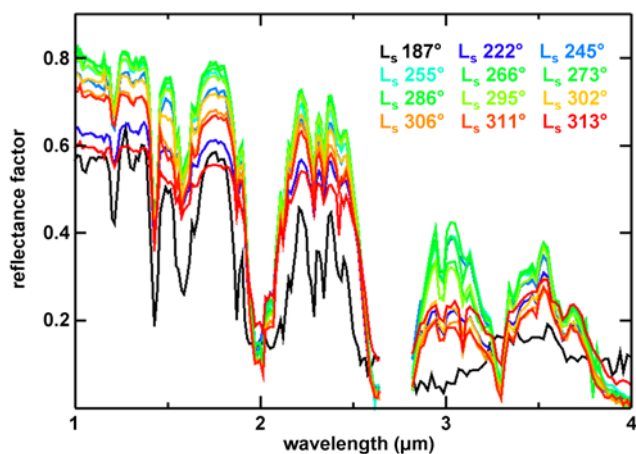


Figure 22. Spectral evolution of a region of the perennial cap at 299°E, 87°S from equinox to the end of the recession. The small and narrow peak at 1.27 μm on the black spectrum (L_s 187°) corresponds to O_2 fluorescence.

and on the surface (southern regions of Hellas). Therefore, in southern winter, the best basis for comparison is provided by the measurements of TES in the thermal IR [Kieffer *et al.*, 2000; Titus, 2005b]. The relationship between the thermal boundary (“Crocus line”) defined by these authors and a boundary of the seasonal cap based on the spectral signatures of CO_2 ice depends on the amount of dust contamination within the ice and on the level of subpixel heterogeneity. Any surface element covered by CO_2 ice will be at 140–145 K, the sublimation temperature of CO_2 in Martian conditions [Kieffer *et al.*, 2000], even with very high levels of dust and H_2O ice contamination of CO_2 ice. In the latter case, these surface elements may present very low CO_2 ice signatures, such as those observed in the cryptic region. Subpixel mixing of ice-covered and ice-free areas is observed at the outer boundaries of the cap. In such cases, the temperature ranges from the temperature of ice-free areas, which is controlled by radiative equilibrium (270 to 240 K for moderate to high solar incidence angles) down to 140–145 K, while $\text{CO}_2(1.435 \mu\text{m})$ ranges from 0% to 60%. From these considerations, we selected a threshold of 20% for $\text{CO}_2(1.435 \mu\text{m})$ when defining the boundary of the CO_2 seasonal cap in Figures 12 to 19. When compared to the temperature criterion of Kieffer *et al.* [2000] and Titus [2005b], this threshold excludes heavily dust contaminated regions (in particular the cryptic region at L_s 223°, which is still covered by CO_2 ice) while including boundary regions with a significant subpixel contribution of CO_2 ice covered areas.

[48] The best fits “Crocus line” contours in 2000 (M-year 25) are derived from Titus [2005b] for the four ranges of heliocentric longitudes presented in Figure 12. They correspond to L_s 90° (for L_s 86°–94.5° in 08/2006, Figure 12a), L_s 133° (for L_s 129.8°–136.2° in 12/2004, Figure 12b), L_s 138° (for L_s 140.9°–154.8° in 01/2005, Figure 12c) and L_s 189° (for L_s 183.9°–192.5° in 03/2005, Figure 12d). The thermal and spectral boundaries are very consistent in terms of longitude distribution. The seasonal cap appears as nearly symmetrical with a northward extension toward Hellas (by 3.5° in latitude at L_s 140°) and toward Argyre (by 2° in

latitude at L_s 150°). The maximum extent (Figure 12a and Figure 12b) in early to midwinter is also very similar as observed by TES in 2000 [Kieffer *et al.*, 2000; Titus, 2005b] and by OMEGA in 2004–2005 (M-year 27). The recession observed by OMEGA in the late southern winter and spring of M-year 27 appears significantly delayed (by ~ 15 days on average, corresponding to 1 to 2.5° in latitude) with respect to the TES observations in 2000 (M-year 25). The full transition from 0% to 30% $\text{CO}_2(1.435 \mu\text{m})$ extends over $\sim 2^\circ$ of latitude so that part of this lag could result from discrepancies between the thermal and spectral criteria.

[49] From the southern spring equinox (Figure 12d) to the end of the recession (Figure 19), the seasonal ice cap is in general much brighter than ice-free areas. This overall brightening of the seasonal cap as the Sun elevation increases was first noted by Paige [1985]. As already discussed, we attribute this brightening to a decrease in the mean grain size combined with a decrease in the optical depth of aerosols. During this part of the seasonal cycle, maps of the southern polar region in the visible were obtained by Mariner 9, Viking and MGS [James *et al.*, 1979, 2001; Kieffer *et al.*, 2000; Benson and James, 2005] over a wide range of Martian years (in particular 1999, 2001 and 2003 with MGS), which provide an excellent basis for comparison with the OMEGA observations in 2005.

[50] The observed evolution of the extent of bright regions is fully in line with previous observations. The development of low-albedo areas soon after equinox with a full-fledged cryptic region at L_s 224° [Kieffer *et al.*, 2000; James *et al.*, 2001] is observed in 2005 (Figure 12d and Figure 13a). The asymmetry of the recession in midspring is well documented in Figure 13 and Figure 14, with a clear role of the cryptic region in triggering a rapid recession from longitudes 60°E to 220°E. The bright region in the mountains of Mitchell area is observed immediately after spring equinox (Figure 12d). Its isolation from the main cap and its sublimation until summer solstice as observed by OMEGA in 2005 are presented in Figures 13 to 15. Shortly before the south summer solstice, there is a very close similarity between the recession in 2005 and that in 1999 and 2003 (Figure 24). The recession in 2001 at L_s 262° as observed by the MOC is significantly faster [Benson and

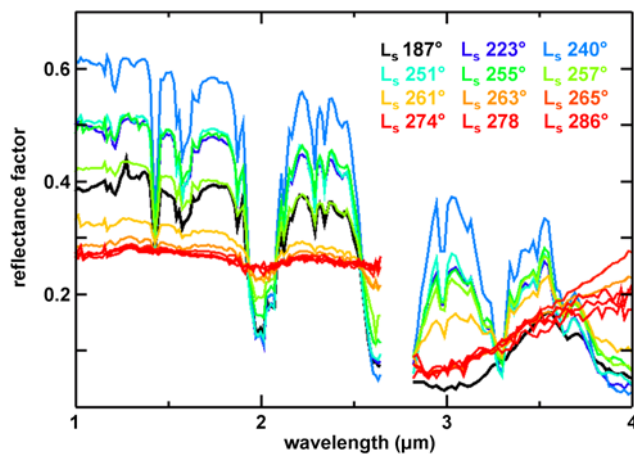


Figure 23. Spectral evolution of a region at 34°E, 76°S. The small and narrow peak at 1.27 μm on the black spectrum (L_s 187°) corresponds to O_2 fluorescence.

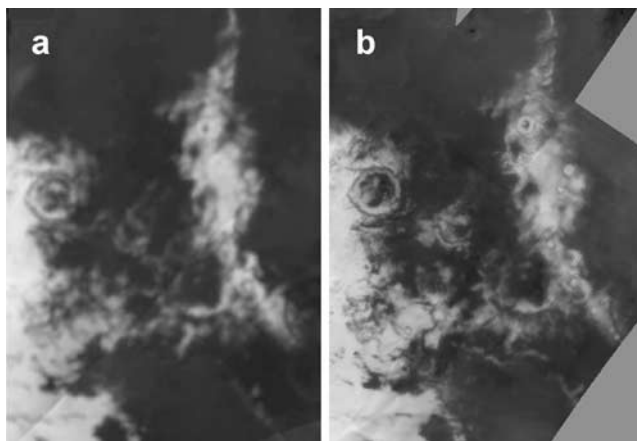


Figure 24. Comparison between (a) an image of the mountains of Mitchell area obtained in the visible by the MOC at L_s 262° in 1999 (Benson and James [2005, Figure 7], with permission from Elsevier) and (b) the albedo map obtained at $1.08 \mu\text{m}$ by OMEGA at L_s 261.6°–263.4° in 2005 adjusted to a similar grey scale (albedo range 0.18–0.65).

James, 2005]. It would correspond to L_s 266.2°–269.8° (Figure 15d) in the OMEGA sequence of observations, a time difference of 7 to 13 days.

[51] For all longitudes from 30°E (mountains of Mitchell) to 220°E (eastern limit of the cryptic region) the recession in terms of regions covered by CO_2 ice is extremely patchy from L_s 223° to L_s 270°. This is in particular the case for the cryptic region itself. This heterogeneity at scales of 10 to 100 km extends down to subpixel scales. Most spectra in these sublimating regions present both significant CO_2 ice spectral features and a large thermal emission contribution. An example of such a spectrum has been presented in Figure 21. Until shortly before the summer equinox, the recession in the other hemisphere is much slower, and the fractal dimension of the sublimation front is much closer to one. This most likely results from a thicker layer of CO_2 ice, related to the difference in weather patterns between these two hemispheres [Colaprete et al., 2005; Montmessin et al., 2004]. After the southern solstice, the overall thickness of the CO_2 layer has been reduced over the whole remaining seasonal cap. The recession is then very rapid between L_s 275° and L_s 290°, with an extremely irregular sublimation front, and widespread occurrences of type I.d spectra over the whole mixing line between ice-covered and ice-free areas at subpixel mixing scales (up to a few hundred meters). Even at such small scales, the surface of surviving patches of CO_2 ice remains relatively clean, as demonstrated by the quality of the areal mixing model for both albedo and band strength presented in Figure 21. The last stages of the CO_2 sublimation process appear very similar in the cryptic region and over the bright cap, but in the latter case the process is delayed by more than two months. Observations at higher resolution by CRISM on board MRO (IFOV: 20 m) will either determine or further constrain the spatial scale of ice-covered and ice-free areas near the sublimation front.

[52] The strong similarity of MOC observations at L_s 306° with the corresponding OMEGA albedo map (Figure 25)

extends to 2005 (M-year 27) the stability of the late stages of the recession over M-years 24, 25 and 26 reported by Benson and James [2005]. Over the last M-years, the recession appears similar to that observed by Viking from 300°E to 40°E. The recession observed from 1999 to 2005 at longitudes from 240°E to 300°E is intermediate between that observed by Viking in 1977 and the faster recession observed by Mariner 9 in 1972. Similarly to earlier phases, regions can appear as relatively homogeneous at the 10 km scale, while exhibiting spatial mixing at subpixel scales, but now there is a third component constituted by H_2O ice – dust mixtures. This is particularly clear when considering the rapid recession during 9 sols of an outlier at 20°E to 40°E, 86°S from L_s 298.9° to L_s 304.4° (Figure 26). Regions extending over several tens of kilometers present an intermediate albedo (0.4 to 0.5), compatible with or marginally higher than bright dust, with clear signatures of CO_2 and H_2O ice and a significant contribution from thermal emission. Figure 27 demonstrates that the spectral evolution of these areas can be interpreted in terms of a changing weight of three subpixels components: CO_2 ice contaminated by dust and H_2O ice, widely observed at L_s 325° in 2006, and very similar to spectra of the perennial cap in 2004 [Bibring et al., 2004a; Douté et al., 2007], a component with relatively weak signatures of H_2O frost admixed with dust (red spectrum from Figure 20b), and an ice free component corresponding to nearby ice-free pixels.

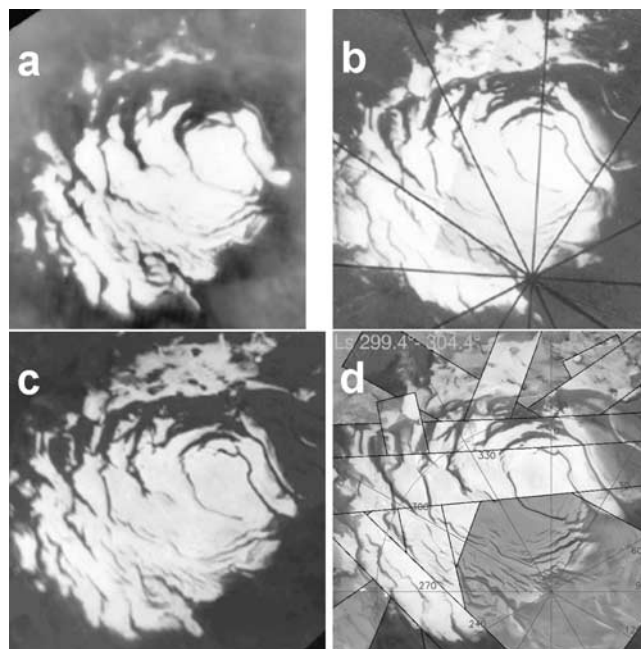


Figure 25. Comparison between three images of the south cap in the visible at L_s 306° (Figures 25a–25c) and the last extended coverage obtained by OMEGA from L_s 299.4° and L_s 304.4° in October 2005 (Figure 19b). The OMEGA mosaic (Figure 25d) has been superimposed on a Viking mosaic obtained after the end of recession so as to position the swaths, which are outlined in black. Figures 25a (Mariner 9, 1972), 25b (Viking, 1977), and 25c (Mars Observer, 2003) are derived from Benson and James [2005, Figures 8 and 9] (with permission from Elsevier) and James et al. [2001].

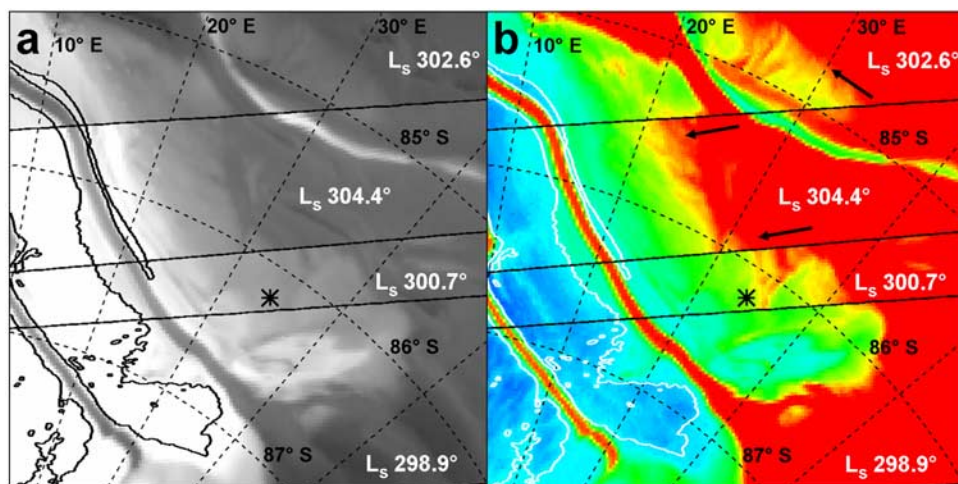


Figure 26. Late stages of the recession of the seasonal cap over a period of 9 sols in a region $160 \text{ km} \times 160 \text{ km}$ at the boundary of the perennial cap: (a) albedo map (black: 0.1; white: 0.6) and (b) CO_2 ice band depth at $1.435 \mu\text{m}$ (red: 0%; dark blue: 60%). This sequence of four OMEGA observations from $L_s 298.9^\circ$ to 304.4° showcases the rapid recession of seasonal CO_2 ice (black arrows) at this period in regions of intermediate albedos (0.4 to 0.5). The white outline is the boundary of the perennial cap as observed by Viking at $L_s 330^\circ$. The 4 km thick ice free strip at center left corresponds to a 7° slope facing N–NE. The IFOF is $\sim 1 \text{ km}$. The area indicated by a star at 34.2°E and 86.2°S is covered by three of the four OMEGA observations ($L_s 298.9^\circ$, $L_s 300.7^\circ$, $L_s 304.4^\circ$). It has been selected for interpreting the spectral evolution of these regions during the last stages of recession.

The ice-free component is responsible for the observed thermal contribution at 4.5 to $5.1 \mu\text{m}$, as any admixture of either CO_2 ice or H_2O ice lowers the temperature below 190 K , with negligible thermal emission in this wavelength range. Over 9 days, the contribution of regions covered by CO_2 ice in the selected area decreases from 73% to 22%, while that covered by H_2O frost admixed with dust rises from 0% to 35% and that of ice-free areas grows from 27% to 43%. Only slightly different combinations of H_2O ice band strengths in the H_2O ice – dust component and H_2O ice contamination of CO_2 ice (which both lower reflectance at $1.5 \mu\text{m}$ and $3 \mu\text{m}$) also provide acceptable fits. In particular, it is not possible to eliminate the H_2O ice – dust component altogether. At $L_s 308.5^\circ$, the H_2O ice – dust component represents $\sim 35\%$ similarly to what was observed at $L_s 304.4^\circ$, while the CO_2 ice component has completely sublimated (65% of the area is ice-free). After $L_s 313.9^\circ$, the whole area is ice-free. The areal mixing at subkilometer scales is likely to be linked with local topography, ice-free areas developing first on north facing slopes, similarly to what can be observed on a larger scale (Figure 26).

4.3. Photometry, Grain Size, and Contamination by Dust and H_2O Ice

[53] The Lambert albedos at $1.08 \mu\text{m}$ measured by OMEGA are consistently higher by ~ 5 to 10% on flat surfaces when compared to that reported by Kieffer *et al.* [2000] from the broadband channel of TES, with a maximum of 0.8 (compared to 0.75) on regions corresponding to the perennial cap and values of 0.7 (compared to 0.6–0.65) for the “bright cap” (longitudes ranging from 320°E to 20°E , latitudes from 75° to 82°). The albedo at $1.08 \mu\text{m}$ is indeed expected to be higher than the average albedo over the 0.3 – $3 \mu\text{m}$ range of the TES broadband bolometer due to

absorption in the UV as well as in near-IR CO_2 ice bands. It should also be noted that a 5% to 10% difference is well within the range expected for uncertainties in absolute photometric calibration of either instrument.

[54] The comparison between the effective grain size determinations in the near IR and the thermal IR is not straightforward. Very small inclusions (such as μm -sized aerosols embedded in ice) provide effective scattering at 1 to $3 \mu\text{m}$ wavelengths, not at $26 \mu\text{m}$, the wavelength range which is used by TES to constrain the effective grain size, or more generally the distance between scattering interfaces. As discussed in section 3.2, the determination of the effective path length within CO_2 ice from OMEGA data in the near IR relies on a simple extinction law, while the TES approach of Kieffer *et al.* [2000] uses model spectra to derive an inverse correlation between effective grain size and band strengths for large grain sizes ($>64 \mu\text{m}$). The evolution of band strength with grain size is not monotonic: The $26 \mu\text{m}$ band strength is the same for grain sizes of $1 \mu\text{m}$ and $256 \mu\text{m}$, and the $26 \mu\text{m}$ band disappears for both very thick CO_2 ice and ice-free surfaces. Notwithstanding these limitations, it is interesting to note that there is significant qualitative agreement between the conclusions of Kieffer *et al.* [2000] and our results, with smaller grain sizes on the perennial cap in summer than on the bright cap. In the latter case, there is even a reasonable quantitative agreement (10 cm from TES, 5 to 10 cm from OMEGA). For regions corresponding to the perennial cap, the transition from a very low band strength at $26 \mu\text{m}$ shortly after equinox to much larger band strengths later in the spring in 1999 is consistent with the transition from type I.a spectra (slab ice) at $L_s \sim 190^\circ$ to type I.c (grain size of a few mm) at $L_s \sim 223^\circ$ observed by OMEGA in 2005.

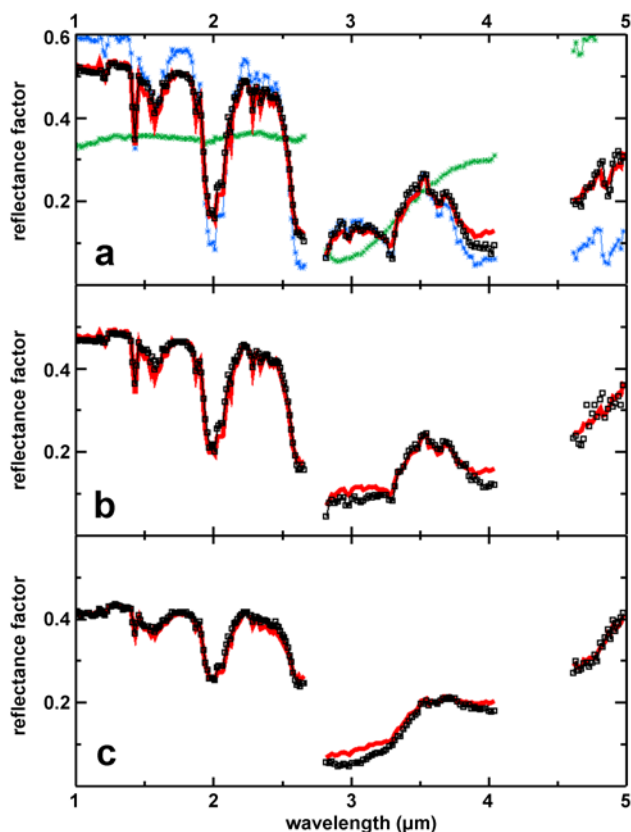


Figure 27. Spectral evolution of the area at 34.2°E and 86.2°S selected in Figure 26 at (a) L_s 298.9°, (b) L_s 300.7°, and (c) L_s 304.4°. These spectra (connected black squares) have been compared to areal mixing models (underlying thick red lines) with three components: a component dominated by CO_2 ice (Figure 19a: blue stars) with significant H_2O ice contamination, an H_2O ice–dust granular mixture (red spectrum from Figure 20b) and an ice-free component (Figure 19a: green stars) selected from a nearby area (35°E , 85.5°S). Model a: $\sim 73\%$ of areal coverage by the CO_2 ice component and $\sim 27\%$ ice-free component; model b: 54% CO_2 ice, 35% ice-free, 11% H_2O ice – dust; model c: 22% CO_2 ice, 43% ice-free, 35% H_2O ice – dust.

[55] The observation of large path lengths in the near-IR combined with high albedo in the continuum lead us to conclude that part of the seasonal cap in spring and summer is composed of remarkably clean CO_2 ice, with upper limits which can be as low as 20 ppm per volume on the contamination by dust and H_2O ice inclusions. There are exceptions at specific times and places, in particular the cryptic region, which presents only weak signatures of CO_2 ice in midspring, and nearby regions which are spectrally dominated by H_2O ice (Figure 13a). The spectral diversity of the cryptic region and its evolution during southern spring has been presented by Langevin *et al.* [2006]. The extensive dust contamination of the surface of CO_2 ice in this region can in part be provided by venting of sub-ice CO_2 bubbles, as proposed by Kieffer [2000], Piqueux *et al.* [2003], and Kieffer *et al.* [2006]. It should however be noted that this dust contamination reduces by a factor of up to

three the solar flux reaching the surface at L_s 223°, reducing the effectiveness of sublimation at the interface between the underlying surface and CO_2 ice. The timing and self-quenching of venting processes must therefore be better understood, as well as alternate sources of dust contamination linked to weather patterns (section 5).

[56] As discussed in sections 3.2 and 3.4, the near IR range provides the most straightforward method for identifying H_2O ice as a surface component. Albedo in the continuum is not a reliable parameter, as CO_2 ice can be as bright or brighter than H_2O ice. Furthermore minor contamination of the surface material by dust can drastically lower the albedo. Such evolutions of the albedo due to dust contamination have been reported by Langevin *et al.* [2005] and are discussed by Vincendon *et al.* [2007]. Sublimation temperatures of H_2O ice in Martian conditions are several tens of kelvins higher than that of CO_2 ice. A bright and moderately cold region (160 to 190 K) is therefore likely to be dominated by H_2O ice. As discussed in the introduction, this made it possible to identify H_2O ice both as the dominant component of the north perennial cap [Kieffer *et al.*, 1976] and in a ring extending over a few degrees of latitude lagging behind the recession of the northern seasonal cap [Kieffer and Titus, 2001]. In both cases, the direct spectral identification by OMEGA confirmed these results; hence the albedo/temperature method has proved quite successful in the past.

[57] The detection of small amounts of H_2O ice as a contaminant of CO_2 ice is not possible from the temperature, as it will remain that of pure CO_2 ice. Given the small difference in indices (1.4 for CO_2 ice, 1.305 for H_2O ice), out of major absorption bands of H_2O ice, reducing the path length of photons in CO_2 ice (effective grain size) requires 20 times more inclusions if the contaminant is H_2O ice when compared to dust [Kieffer and Titus, 2001]. In contrast, detecting such contaminants is relatively straightforward in the near-IR due to the impact of absorption bands on reflectance factors. This made it possible to follow the evolution of H_2O contamination of CO_2 ice during the recession of the seasonal cap. During southern winter, most of the H_2O signatures are observed in relationship with Hellas. At winter solstice, a H_2O frost reservoir has accumulated in the southern parts of the basin (Figure 12a), with a transition from pure H_2O frosts (type III) to H_2O contamination of CO_2 ice (type II). As we get closer to equinox, the contamination spreads eastward (Figures 12b and 11c). Shortly after equinox (Figure 12d), H_2O frost has sublimated from Hellas, and H_2O contamination is widespread in the polar cap. The signatures are too strong at $1.5 \mu\text{m}$ to correspond only to H_2O ice clouds. It is interesting to note that the strong $1.5 \mu\text{m}$ signatures are nearly all included within the boundaries of the CO_2 ice cap (dark outline on the H_2O ice map) except within or close to the Hellas basin. The low levels at $3 \mu\text{m}$ (e.g., in the green spectrum of Figure 20c) indicate that there is both a relatively large grained H_2O ice component as a contaminant of CO_2 ice and a contribution from H_2O ice clouds. The situation in midspring is quite specific, with well identified patches close to the cryptic region where CO_2 ice is strongly contaminated by H_2O ice (500 ppm or more and a significant reduction in the extent of both surface contamination and cloud activity as monitored by the $3.4 \mu\text{m}/3.52 \mu\text{m}$ ratio. The

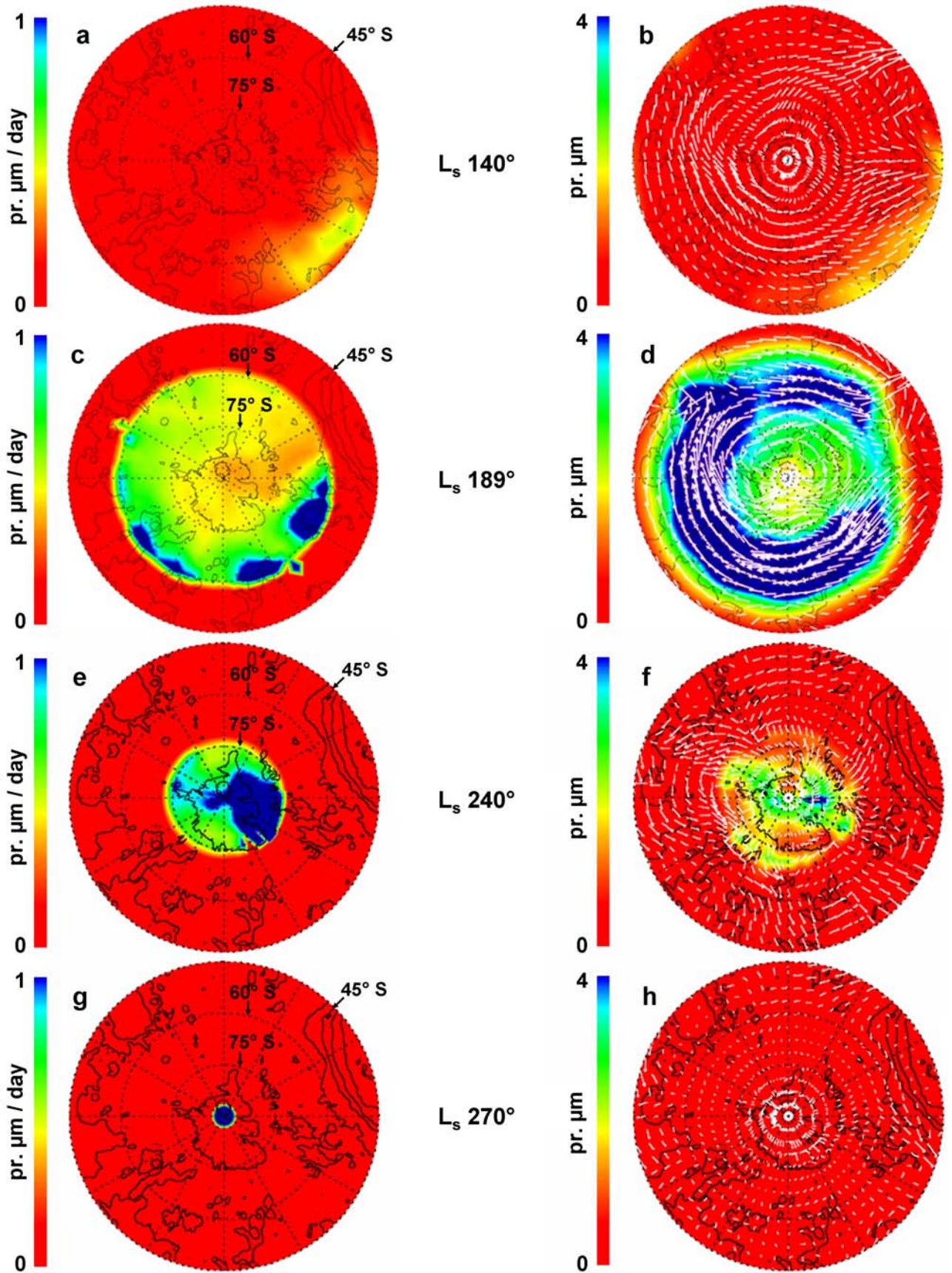


Figure 28

results on H₂O ice clouds will be further discussed in section 5 together with the results of general climate models.

[58] Very few H₂O ice patches have been observed by OMEGA in late spring and early summer either as contamination of CO₂ ice or outside the CO₂ seasonal cap. The largest such feature, at 127°E, 77°S, is first identified in midspring as one of the areas spectrally dominated by H₂O ice close to the cryptic region (Figure 13a). It survives until L_s 254°, more than one month after the sublimation of CO₂ (Figure 14b). This is in sharp contrast to the nearly continuous H₂O frost ring observed around the north seasonal cap in early to mid northern spring. In 2005, we do not observe any significant H₂O ice signature at L_s 270°, a value of L_s for which a small H₂O frost covered region was inferred at 156°E, 86.4°S from TES/THEMIS observations in 2003 using the same albedo/temperature approach as in the north [Titus, 2005a]. It is possible that this feature is not present every Martian year. However, in 2005, OMEGA observes a behavior of this area in terms of albedo and temperatures which is very similar to that reported by Titus [2005a]. The observed spectra in 2005 are consistent with subpixel mixing of CO₂ frost and ice-free areas. As discussed in the previous section, subpixel mixing between CO₂ ice and ice-free areas, with no remaining veneer of H₂O frost, seems to be the nominal situation for the last stages of sublimation in the south, even in surviving “islands” or “peninsulas” such as that at 156°E, 86.4°S.

[59] From L_s 240° to L_s 290°, the whole CO₂ cap is nearly free of large-grained H₂O contributions. No significant contribution from H₂O ice in clouds is observed. The few signatures in terms of the 3.4 μm/3.52 μm ratio can be interpreted as resulting from a large CO₂ effective grain size: the 3 μm level is larger than that at 3.4 μm, with a well developed 3.3 μm absorption band. These spectral characteristics are incompatible with a small-grained H₂O ice signature.

[60] From L_s 290° to the end of the recession, the contribution of H₂O ice becomes again significant. The spectral signatures at 1.5 μm and the rapid albedo decrease from ~0.8 to ~0.6 over areas corresponding to the perennial cap (Figure 18) requires contamination by both H₂O ice and dust with a level of several 0.01 wt%, as discussed by Bibring *et al.* [2004a] and Douté *et al.* [2007]. Macroscopic and subpixel patches dominated by mixtures of H₂O ice and dust are observed close to the sublimation front, as discussed in section 4.2, then close to the outer edge of the perennial cap and as an arc at 83.5°S between 320° and 20°, confirming the observations in 2004 [Bibring *et al.*, 2004a].

5. Comparison Between the Evolution of H₂O Ice Signatures and Model Predictions

[61] So as to better understand the spatial distribution and time variation of H₂O frost signatures, it is interesting to compare the OMEGA observations with the results of a

Martian general circulation model (GCM). We used the GCM developed at the Laboratoire de Météorologie Dynamique [Forget *et al.*, 1999] which is able to simulate the atmospheric water cycle [Montmessin *et al.*, 2004] by taking into account the exchanges between surface ice and the atmosphere as well as the transport and turbulent mixing of water, relying on simplified microphysics for cloud formation. It provides distributions of H₂O gas and ice clouds in good agreement with MGS TES observations [Montmessin *et al.*, 2004]. Figure 28 (left) shows 10-day averaged H₂O ice deposition rates at L_s 140°, L_s 189°, L_s 240° and L_s 270°, providing an estimate of the amount of recently deposited H₂O ice grains which can be observed on the surface by OMEGA. The agreement on the location of preferred H₂O ice deposition regions is very good at L_s ~ 140° (Figure 28a) and L_s ~ 189° (Figure 28c). The model predicted that the deposition of water ice should not be axi-symmetric and should occur preferentially east of Hellas, which is confirmed by OMEGA observations. Out of Hellas, H₂O ice deposition is constrained within the boundaries of the seasonal cap in late southern winter and early southern spring, in good agreement with OMEGA observations. The H₂O ice reservoir in Hellas was already present at L_s 90° in OMEGA data, and it is still observed at L_s 140°. It does not show up in the H₂O ice surface accumulation map at 140°. This behavior can be explained by the weather patterns of Figure 28 (right) which shows the horizontal wind vectors around 2 km above the surface along with a map of the water ice clouds. In late winter, H₂O ice sublimates within Hellas (hence a negative accumulation rate, and a red color in the model maps). The dominant factor in water ice deposition appears to be the injection of relatively water-rich air in the eastward polar vortex by a strong southward flow east of Hellas. This flow results from a stationary wave forced by the stretching of vortex tubes as air passes over the Hellas topographic depression which dominates the high-latitude southern hemisphere atmospheric circulation during fall, winter and spring until around L_s = 230° in our simulation. Such a flow had been evoked to explain the injection of relatively warm air in the eastern south polar night in winter [Colaprete *et al.*, 2005]. Conversely an equatorward flow forms on the western side of Hellas, driving cold, dry air out of the polar region. At L_s 189°, the widespread contamination of the CO₂ ice cap by minor amounts of H₂O frost can be interpreted from the recondensation of H₂O released by sublimation of frost at lower latitudes [Houben *et al.*, 1997]. The area south of Hellas is somewhat isolated between the two flows mentioned above and remains relatively free of surface ice in both the observations and the GCM simulations (Figure 29).

[62] At L_s 189° (Figure 28d), significant H₂O ice cloud activity is expected up to 10° in latitude beyond the boundaries of the CO₂ cap which constitutes a discrepancy with the OMEGA results. A map of the 3.4 μm to 3.52 μm

Figure 28. Ten day averaged maps (left) of H₂O ice accumulation on the surface and (right) of the atmospheric H₂O ice cloud content predicted by the GCM of Forget *et al.* [1999] and Montmessin *et al.* [2004] for four values of L_s corresponding to sets of OMEGA observations. The length and direction of white arrows on the right correspond to wind speeds and directions predicted by the model. Several tens of μm can be accumulated in a few weeks at favorable locations; 3 μm of precipitable water corresponds to a H₂O ice band depth of more than 10% at 1.5 μm (depending on particle size) which should be observed by OMEGA.

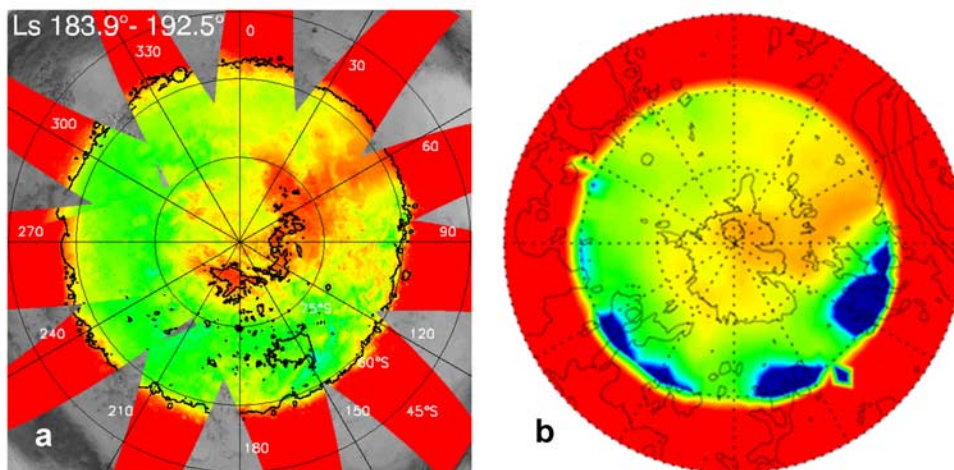


Figure 29. (a) Map of the H_2O ice signature at $1.5 \mu\text{m}$ observed by OMEGA shortly after equinox, from Figure 12d. Surface ice is mainly restricted to the CO_2 ice cap (black outline). (b) model predictions (from Figure 28c) The extent in latitude and the longitudinal distribution of surface ice contamination are well reproduced by the model, in particular the “dry spoke” at $\sim 60^\circ\text{E}$, south of the Hellas basin.

ratio obtained by OMEGA shortly after equinox is shown in Figure 30. The $3 \mu\text{m}$ -sized H_2O ice signature ($3 \mu\text{m}$ feature, Figure 30a) extends farther out than the $1.5 \mu\text{m}$ signature corresponding to larger grain sizes (Figure 29a), which is mostly constrained within the CO_2 ice cap. These extensions beyond the cap are mainly observed from 180°E to

350°E , which is consistent with the longitudinal distribution predicted by the model (Figure 28d), but they do not exceed a few degrees in latitude, which falls far short of model predictions ($\sim 10^\circ$ farther north than the boundary of the seasonal cap). At $L_s 240^\circ$, there is also some discrepancy between models and observations as very little H_2O ice is

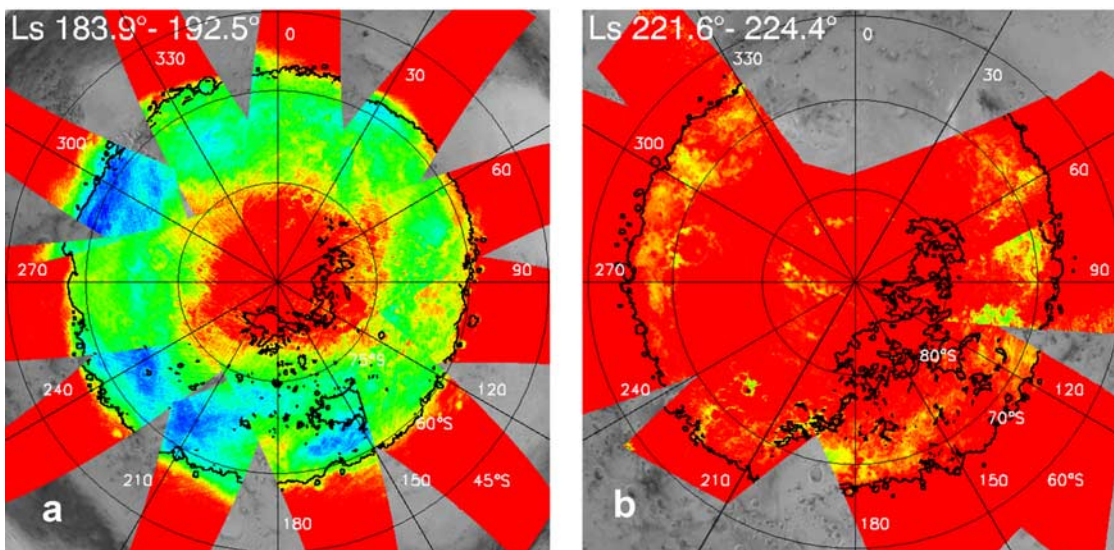


Figure 30. Map of the $3.4 \mu\text{m}/3.525 \mu\text{m}$ ratio observed by OMEGA (a) shortly after equinox and (b) in midspring. At latitudes higher than 85°S , the air mass is very large (10 to 15) shortly after equinox, so that even weak signatures of H_2O ice in clouds should have a major impact on the $3 \mu\text{m}$ spectral region. The low ratio in outer regions of Figure 30a corresponds to a contribution from clouds. The overlap mismatches between the swath at 270°E ($L_s 191^\circ$), the underlying swath ($L_s 183.9^\circ$), and swaths at 240°E ($L_s 185^\circ$) or 300°E ($L_s 187^\circ$) are consistent with a variable H_2O ice content in the atmosphere. The lower amount of water ice at high southern latitudes is well reproduced by the model (Figure 30b, from Figure 28d, $L_s 189^\circ$). In midspring, the $3.4 \mu\text{m}/3.525 \mu\text{m}$ ratio is high except for a few well-defined regions with large CO_2 grain sizes (e.g., at 276°E , 70°S and 300°E , 68°S) or large contributions from surface H_2O frost (e.g., at 200°E and 226°E , 73°S ; see Figure 13a). Spectra from these areas do not require a significant contribution from icy cloud signatures except possibly for the patch at 75°E , 70°S .

observed either on the ground or in the atmosphere after mid-spring (Figure 30b) while the model predicts both significant frost accumulation and H₂O ice aerosol activity at latitudes higher than 74°S. The OMEGA results demonstrate that the recondensation process of sublimating water ice at higher latitudes [Houben *et al.*, 1997] which was responsible for widespread H₂O ice contamination close to the southern spring equinox is not observed during the recession in late spring and early summer, due to the very small amount of available H₂O. At L_s 270° (Figures 28g and 28h), the model predicts virtually no ice accumulation and a very low content of H₂O ice in the atmosphere, in very good agreement with observations.

[63] Even if there are a few discrepancies, the overall qualitative agreement between the model and the OMEGA observations is quite satisfactory. In particular, the time evolution of H₂O ice aerosol activity as observed by OMEGA, with a strong peak close to the southern equinox and low levels in winter as well as close to the summer solstice is very well accounted for. With up to 4 μm of integrated ice column densities in the atmosphere, one would expect stronger absorptions at 1.5 μm than those observed by OMEGA as diffuse signatures. These lower extinctions could result from the presence of dust cores within H₂O ice grains (heterogeneous nucleation) as discussed by Bell *et al.* [1996] for CO₂ ice grains. The longitudinal distributions and seasonal variations of H₂O ice accumulation rates on the surface are very consistent with OMEGA observations. A quantitative comparison between these accumulation rates and the observed surface H₂O ice signatures would require a comprehensive modeling of the life cycle of the deposited H₂O ice grains within and at the surface of CO₂ ice, then as frost veneers or intimate mixtures with surface dust.

6. Conclusions

[64] The observations performed by OMEGA from 2004 to 2006 cover the evolution of the southern seasonal cap from the southern winter solstice (shortly before the period of maximum extension of the cap, at L_s 115°) to the end of the recession, at L_s 325°. The albedo in the continuum and specific spectral signatures of H₂O ice (at 1.5 μm) and CO₂ ice (at 1.435 μm) have been used to characterize the extent and evolution of the seasonal cap in terms of the equivalent grain size of CO₂ ice, contamination by H₂O ice and dust. Extensive coverage was obtained for three periods in southern winter and one period shortly after spring equinox. A series of 26 maps were obtained in 2005 from L_s 223° (mid southern spring) to L_s 325° (end of the recession of the seasonal cap), at intervals of one week on average, with IFOVs ranging from ~10 km at the beginning of the period to 1 km at the end of the recession. For selected regions of interests, the local evolution of the seasonal cap in terms of equivalent grain size of CO₂ ice, dust and H₂O contamination, subpixel contributions of ice free areas can further be analyzed by extracting temporal series of spectra, with a minimum interval of 3 sols with the same observation geometry. The contributions of surface H₂O frost and that of μm-sized H₂O ice aerosols could be discriminated from the band strength and shape at 3 μm, which is very strong relative to absorptions at 1.5 μm and 2 μm for small icy grains in transmission. This data set provides the most

comprehensive information to date on the recession of the southern seasonal cap.

[65] During southern winter, the regions presenting strong CO₂ ice signatures are nearly isotropically distributed, confirming previous results in the thermal IR [Kieffer, 1979; Kieffer *et al.*, 2000], and their boundary closely matches that of regions close to CO₂ ice sublimation temperatures in 2001 [Titus, 2005b]. This could result in part from a slower recession in 2005, even if CO₂ ice signatures are expected to extend beyond the temperature limit due to subpixel mixing with hot ice free areas along the sublimation front. Most of the southern seasonal cap is characterized by very large grain sizes and a weak albedo contrast between ice-covered and ice-free regions, which require a very clean CO₂ ice layer (“slab ice”) so that most photons reach the underlying surface in the continuum. At winter solstice, in sharp contrast to the north seasonal cap, the south seasonal cap is nearly free of H₂O ice contamination except to regions within or close to Hellas. After L_s 115°, H₂O ice contamination extends eastward until shortly after equinox, when the seasonal cap is contaminated over all longitudes except for a “dry spoke” close to 60°E. This behavior can be attributed to the H₂O ice sublimation-recondensation process initially proposed by Houben *et al.* [1997]. At L_s ~ 190°, contamination by H₂O frost on the surface is associated with a weak, widespread icy aerosol contribution at latitudes northward of 75°S, which extend slightly beyond the edge of the seasonal cap.

[66] After equinox, the seasonal cap is in general much brighter than surrounding terrains. OMEGA observations reveal that the albedo and spectral evolution during spring and summer results from a wide range of processes, involving changes in effective grain size of the CO₂ ice, in the aerosol optical thickness, in surface dust contamination and subpixel spatial mixing of ice-covered and ice-free areas during the final stages of the sublimation of a region of the seasonal cap. The increase in albedo of the regions corresponding to the perennial cap after equinox correspond to a major decrease in effective grain size, while the albedo decreases close to the end of the recession due to contamination of CO₂ ice by dust. The low albedo of the cryptic region results from extensive dust contamination of the surface [Langevin *et al.*, 2006], which could result to a large extent to venting of sub-ice gas bubbles as proposed by Kieffer [2000], Piqueux *et al.* [2003], and Kieffer *et al.* [2006]. The seasonal cap boundary rapidly recessions at longitudes corresponding to the cryptic region (60°E to 220°E) from L_s 230° to L_s 250° and at longitudes 300°E to 30°E from L_s 270° to L_s 290°. During such phases, regions presenting macroscopic and subpixel mixing of ice-covered and ice-free areas can extend over several hundred km, with a very complex sublimation front.

[67] Very little H₂O ice is observed in aerosols from late southern spring to the end of the recession. Neither contamination of CO₂ ice by H₂O ice nor extensive H₂O frost patches out of the CO₂ seasonal cap are observed from L_s 240° to L_s 290°. The recondensation process of Houben *et al.* [1997] which was very active until early southern spring is not observed during the rapid recession of the seasonal cap around the southern summer solstice. Contamination by H₂O ice begins to be observed again shortly before L_s 300°.

It reaches a maximum at L_s 310°, and it is still present at a lower level over the perennial cap after the end of the recession, together with a few patches of H₂O frost mixed with dust contiguous to the perennial cap, confirming the results of Bibring *et al.* [2004a] and Douté *et al.* [2007]. Spectra observed during the last stages of the recession close to the sublimation front require subpixel mixing with three components: CO₂ ice contaminated at levels of a few 0.01 wt% by H₂O ice and dust, an H₂O ice – dust granular mixture and ice-free areas. High-resolution observations with CRISM on board MRO (IFOV: 30 m) will be able to resolve areal mixing cases with either two component (CO₂ ice, ice-free) or three component (CO₂ ice, H₂O ice – dust mixture, ice-free) areal mixing situations if the extent of homogeneous areas is larger than a few tens of meters.

[68] The predictions of the general circulation model of Montmessin *et al.* [2004] and Forget *et al.* [2005] provide a good qualitative interpretation of the observations of H₂O ice on the ground and in the atmosphere, with a major role of weather systems originating in Hellas [Colaprete *et al.*, 2005]. The peak in ice cloud activity close to the southern spring equinox is predicted, as well as the very low level of H₂O ice on the ground or in the atmosphere close to the southern summer solstice. Resolving the remaining discrepancies (extent of icy aerosols close to equinox, H₂O ice activity at high southern latitudes predicted but not observed at L_s 240°) will require adjusting the assumptions and the input parameters of global circulation models. Therefore the OMEGA observations of the recession of the southern seasonal cap constitute a significant step toward a better understanding of the water cycle on Mars.

References

- Bell, J. F., III, W. M. Calvin, M. E. Ockert-Bell, D. Crisp, J. B. Pollack, and J. Spencer (1996), Detection and monitoring of H₂O and CO₂ ice clouds on Mars, *J. Geophys. Res.*, *101*, 9227–9237.
- Benson, J. L., and P. B. James (2005), Yearly comparisons of the Martian polar caps: 1999–2003 Mars Orbiter Camera observations, *Icarus*, *174*, 513–523.
- Bibring, J.-P., et al. (2004a), Perennial water ice identified in the south polar cap of Mars, *Nature*, *428*(6983), 627–630.
- Bibring, J.-P., et al. (2004b), OMEGA: Observatoire pour la Minéralogie, l'Eau, les Glaces et l'Activité, in *Mars Express: The Scientific Payload*, edited by A. Wilson, *Eur. Space Agency Spec. Publ.*, ESA-I240, 37–49.
- Bibring, J.-P., et al. (2005), Mars surface diversity as revealed by the OMEGA/Mars Express observations, *Science*, *307*, 1576–1581.
- Calvin, W. M., and T. Z. Martin (1994), Spatial variability in the seasonal south polar cap of Mars, *J. Geophys. Res.*, *99*, 21,143–21,152.
- Clancy, R. T., and B. J. Sandor (1998), CO₂ ice clouds in the upper atmosphere of Mars, *Geophys. Res. Lett.*, *25*, 489–492.
- Clancy, R. T., M. J. Wolff, and P. R. Christensen (2003), Mars aerosol studies with the MGS TES emission phase function observations: Optical depths, particle sizes, and ice cloud types versus latitude and solar longitude, *J. Geophys. Res.*, *108*(E9), 5098, doi:10.1029/2003JE002058.
- Colaprete, A., J. R. Barnes, R. M. Haberle, M. Robert, J. L. Hollingsworth, H. H. Kieffer, and T. N. Titus (2005), Albedo of the south pole on Mars determined by topographic forcing of atmosphere dynamics, *Nature*, *435*, 184–188.
- Douté, S., and B. Schmitt (1998), A multilayer bidirectional reflectance model for the analysis of planetary surface hyperspectral images at visible and near-infrared wavelengths, *J. Geophys. Res.*, *103*, 31,367–31,390.
- Douté, S., B. Schmitt, Y. Langevin, J.-P. Bibring, F. Altieri, G. Bellucci, B. Gondet, F. Poulet, and MEX OMEGA Team (2007), South Pole of Mars: Nature and composition of the icy terrains from Mars Express OMEGA observations, *Planet. Space Sci.*, *55*(1–2), 113–133.
- Erard, S., J. Mustard, S. Murchie, J.-P. Bibring, P. Cerroni, and A. Coradini (1994), Martian aerosols: Near-IR spectral properties and effects on the observation of the surface, *Icarus*, *111*, 317–337.
- Forget, F., F. Hourdin, R. Fournier, C. Hourdin, O. Talagrand, M. Collins, R. L. Stephens, P. L. Read, and J.-P. Huot (1999), Improved general circulation models of the Martian atmosphere from the surface to above 80 km, *J. Geophys. Res.*, *104*, 24,155–24,176.
- Forget, F., B. Levrard, F. Montmessin, B. Schmitt, S. Douté, Y. Langevin, and J.-P. Bibring (2005), Mars water ice and carbon dioxide seasonal polar caps: GCM modelling and comparison with Mars Express OMEGA observations, *Proc. Lunar Planet. Sci. Conf.* 36th, Abstract 1605.
- Glenar, D. A., R. E. Samuelson, J. C. Pearl, G. L. Bjoraker, and D. Blaney (2003), Spectral imaging of Martian water ice clouds and their diurnal behavior during the 1999 aphelion season ($L_s = 130^\circ$), *Icarus*, *161*, 297–318.
- Gondet, B., J.-P. Bibring, Y. Langevin, F. Poulet, F. Montmessin, and F. Forget (2006), One Martian year observation of H₂O ice clouds by OMEGA/Mars Express, paper presented at Second Workshop on Mars Atmosphere Modelling and Observations, Cent. Natl. d'Etudes Spatiales, Granada, Spain.
- Grundy, W. M., and B. Schmitt (1998), The temperature-dependent near-infrared absorption spectrum of hexagonal H₂O ice, *J. Geophys. Res.*, *103*, 25,809–25,822.
- Hansen, G. B. (2005), Ultraviolet to near-infrared absorption spectrum of carbon dioxide ice from 0.174 to 1.8 μm , *J. Geophys. Res.*, *110*, E11003, doi:10.1029/2005JE002531.
- Herr, K. C., and G. C. Pimentel (1969), Infrared absorptions near three microns recorded over the polar caps of Mars, *Science*, *166*, 496–499.
- Houben, H., R. M. Haberle, R. E. Young, and A. P. Zent (1997), Modeling the Martian seasonal water cycle, *J. Geophys. Res.*, *102*, 9069–9084.
- James, P. B., G. Briggs, J. Barnes, and A. Spruck (1979), Seasonal recession of Mars' south polar cap as seen by Viking, *J. Geophys. Res.*, *84*, 2889–2922.
- James, P. B., K. M. Malolepszy, and L. J. Martin (1987), Interannual variability of Mars' south polar cap, *Icarus*, *71*, 298–305.
- James, P. B., H. H. Kieffer, and D. E. Paige (1992), The seasonal cycle of carbon dioxide on Mars, in *Mars*, edited by H. H. Kieffer et al., pp. 934–968, Univ. of Ariz. Press, Tucson.
- James, P. B., B. A. Cantor, and S. Davis (2001), Mars Orbiter Camera observations of the Martian south polar cap in 1999–2000, *J. Geophys. Res.*, *106*, 23,635–23,652.
- Jakosky, B. M. (1985), The seasonal cycle of Mars, *Space Sci. Rev.*, *41*, 131–200.
- Jouglet, D., F. Poulet, J. Mustard, R. Milliken, J.-P. Bibring, Y. Langevin, and B. Gondet (2007), Observation of the 3 μm hydration feature on Mars from OMEGA/Mars Express data, *J. Geophys. Res.*, doi:10.1029/2006JE002846, in press.
- Kieffer, H. H. (1979), Mars south polar spring and summer temperatures: A residual CO₂ frost, *J. Geophys. Res.*, *84*, 8263–8288.
- Kieffer, H. H. (2000), Annual punctuated CO₂ slab-ice and jets on Mars, in *Second International Conference on Mars: Polar Science and Exploration*, p. 93, Lunar and Planet. Inst., Houston, Tex.
- Kieffer, H. H., and T. N. Titus (2001), TES mapping of Mars' north seasonal cap, *Icarus*, *154*, 162–180.
- Kieffer, H. H., S. C. Chase, T. Z. Martin, R. E. Miner, and F. D. Palluconi (1976), Martian North Pole summer temperatures—Dirty water ice, *Science*, *194*, 1341–1344.
- Kieffer, H. H., T. N. Titus, K. F. Mullins, and P. R. Christensen (2000), Mars south polar spring and summer behavior observed by TES: Seasonal cap evolution controlled by frost grain size, *J. Geophys. Res.*, *105*, 9653–9700.
- Kieffer, H. H., P. R. Christensen, and T. M. Titus (2006), CO₂ jets formed by sublimation beneath translucent slab ice in Mars' seasonal south polar ice cap, *Nature*, *442*, 793–796.
- Langevin, Y., F. Poulet, J.-P. Bibring, B. Schmitt, S. Douté, and B. Gondet (2005), Summer evolution of the North Polar Cap of Mars as observed by OMEGA/Mars Express, *Science*, *307*, 1581–1583.
- Langevin, Y., S. Douté, M. Vincendon, F. Poulet, J.-P. Bibring, B. Gondet, B. Schmitt, and F. Forget (2006), No signature of clear CO₂ ice from the 'cryptic' regions in Mars' south seasonal polar cap, *Nature*, *442*, 831–835.
- Larson, H. P., and U. Fink (1972), Identification of carbon dioxide frost on the Martian polar caps, *Astrophys. J.*, *171*, L91–L95.
- Milliken, R. E., J. F. Mustard, F. Poulet, D. Jouglet, J.-P. Bibring, B. Gondet, and Y. Langevin (2007), Hydration state of the Martian surface as seen by Mars Express OMEGA II: H₂O content of the surface, *J. Geophys. Res.*, doi:10.1029/2006JE002853, in press.
- Montmessin, F., F. Forget, P. Rannou, M. Cabane, and R. M. Haberle (2004), Origin and role of water ice clouds in the Martian water cycle as inferred from a general circulation model, *J. Geophys. Res.*, *109*, E10004, doi:10.1029/2004JE002284.
- Montmessin, F., et al. (2006), Subvisible CO₂ ice clouds detected in the mesosphere of Mars, *Icarus*, *183*, 403–410.
- Neugebauer, G., G. Munch, H. H. Kieffer, S. C. Chase Jr., and E. D. Miner (1971), Mariner 1969 infrared radiometer results: Temperatures and thermal properties of the Martian surface, *Astron. J.*, *76*, 719–749.

- Neumann, G. A., D. E. Smith, and M. T. Zuber (2003), Two Mars years of clouds detected by the Mars Orbiter Laser Altimeter, *J. Geophys. Res.*, *108*(E4), 5023, doi:10.1029/2002JE001849.
- Ockert-Bell, M. E., J. F. Bell III, J. B. Pollack, C. P. McKay, and F. Forget (1997), Absorption and scattering properties of the Martian dust in the solar wavelengths, *J. Geophys. Res.*, *102*(E4), 9039–9050.
- Paige, D. A. (1985), The annual heat balance of the Martian polar caps from Viking observations, Ph.D. thesis, Calif. Inst. of Technol., Pasadena, Calif.
- Paige, D. A., and K. D. Keegan (1994), Thermal and albedo mapping of the polar regions of Mars using Viking thermal mapper observations: 2. South polar region, *J. Geophys. Res.*, *99*, 25,993–26,013.
- Piqueux, S., S. Byrne, and M. I. Richardson (2003), Sublimation of Mars's southern seasonal CO₂ ice cap and the formation of spiders, *J. Geophys. Res.*, *108*(E8), 5084, doi:10.1029/2002JE002007.
- Poulet, F., J. N. Cuzzi, D. P. Cruikshank, T. Roush, and C. M. Dalle Ore (2002), Comparison between the Shkuratov and Hapke scattering theories for solid planetary surfaces: Application to the surface composition of two centaurs, *Icarus*, *160*(2), 313–324.
- Quirico, E., and B. Schmitt (1997), Near-infrared spectroscopy of simple hydrocarbons and carbon oxides diluted in solid N₂ and as pure ices: Implications for Triton and Pluto, *Icarus*, *127*, 354–378.
- Schmitt, B., S. Douté, Y. Langevin, F. Forget, J.-P. Bibring, B. Gondet, and OMEGA Team (2005), Northern seasonal condensates on Mars by OMEGA/Mars Express, *Proc. Lunar Planet. Sci. Conf. 36th*, Abstract 2326.
- Shorghofer, N., and K. S. Edgett (2006), Seasonal surface frost at low latitudes on Mars, *Icarus*, *180*, 321–334.
- Smith, M. D., C. J. Pearl, B. J. Conrath, and P. R. Christensen (2001), Thermal Emission Spectrometer results: Mars atmospheric thermal structure and aerosol distribution, *J. Geophys. Res.*, *106*, 23,929–23,945.
- Smith, M. D., J. L. Bandfield, P. R. Christensen, and M. I. Richardson (2003), Thermal Emission Imaging System (THEMIS) infrared observations of atmospheric dust and water ice cloud optical depth, *J. Geophys. Res.*, *108*(E11), 5115, doi:10.1029/2003JE002115.
- Titus, T. N. (2005a), Thermal infrared and visual observations of a water ice lag in the Mars southern summer, *Geophys. Res. Lett.*, *32*, L24204, doi:10.1029/2005GL024211.
- Titus, T. N. (2005b), Mars Polar cap edges tracked over 3 full Mars years, *Proc. Lunar Planet. Sci. Conf. 36th*, Abstract 1993.
- Titus, T. N., and H. H. Kieffer (2002), A comparison of the Mars south polar recession rates between 1999 and 2001, *Proc. Lunar Planet. Sci. Conf. 33rd*, Abstract 2071.
- Vincendon, M., Y. Langevin, F. Poulet, J.-P. Bibring, B. Gondet, B. Schmitt, and S. Douté (2006), Surface water ice and aerosols evolution of 77°N, 90°E Mars crater during early summer by OMEGA/Mex, *Proc. Lunar Planet. Sci. Conf. 37th*, Abstract 1769.
- Vincendon, M., Y. Langevin, F. Poulet, J.-P. Bibring, and B. Gondet (2007), Recovery of surface reflectance spectra and evaluation of the optical depth of aerosols in the near-IR using a Monte Carlo approach: Application to the OMEGA observations of high-latitude regions of Mars, *J. Geophys. Res.*, doi:10.1029/2006JE002845, in press.
- Wang, H., and A. P. Ingersoll (2002), Martian clouds observed by Mars Global Surveyor Mars Orbiter Camera, *J. Geophys. Res.*, *107*(E10), 5078, doi:10.1029/2001JE001815.
- Warren, S. G. (1986), Optical constants of carbon dioxide ice, *Appl. Opt.*, *25*, 2650–2674.

J.-P. Bibring, B. Gondet, Y. Langevin, F. Poulet, and M. Vincendon, Institut d'Astrophysique Spatiale, CNRS/Université Paris Sud, Bâtiment 120, F-91405, Orsay, France. (yves.langevin@ias.u-psud.fr)

S. Douté, Laboratoire de Planetologie de Grenoble, CNRS/Université Joseph Fourier, BP 53, F-38041 Grenoble Cedex 9, France.

F. Forget, Laboratoire de Météorologie Dynamique, CNRS/Université Pierre et Marie Curie, Case Postale 99, 4 Place Jussieu, F-75252 Paris Cedex 05, France.

F. Montmessin, Service d'Aéronomie, CNRS/Université Pierre et Marie Curie, Tour 45, Couloir 45-46, 3e et 4e Etage (Boîte 102), 4 Place Jussieu, F-75252 Paris Cedex 05, France.